Solar Sails and Lunar South Pole Coverage

M. T. Ozimek,* D. J. Grebow,* K. C. Howell†
Purdue University, West Lafayette, IN, 47907-2045, USA

Potential orbits for continuous surveillance of the lunar south pole with just one spacecraft and a solar sail are investigated. Periodic orbits are first computed in the Earth-Moon Restricted Three-Body Problem, using Hermite-Simpson and seventh-degree Gauss-Lobatto collocation schemes. The schemes are easily adapted to include path constraints favorable for lunar south pole coverage. The methods are robust, generating a control history and a nearby solution with little information required for an initial guess. Five solutions of interest are identified and, using collocation, transitioned to the full ephemeris model (including the actual Sun-to-spacecraft line and lunar librations). Of the options investigated, orbits near the Earth-Moon L_2 point yield the best coverage results. Propellant-free transfers from a geosynchronous transfer orbit to the coverage orbits are also computed. A steering law is discussed and refined by the collocation methods. The study indicates that solar sails remain a feasible option for constant lunar south pole coverage.

Nomenclature

$\boldsymbol{x}$	State Variable Vector
t	Time
$\boldsymbol{u}$	Control Variable Vector
$\boldsymbol{r}, \boldsymbol{v}$	Position and Velocity Vectors, Earth-Moon Rotating Frame
U	Potential Function
$\boldsymbol{a}$	Sail Acceleration Vector
$\boldsymbol{R}, \boldsymbol{V}$	Position and Velocity Vectors, EMEJ2000 Frame
$\boldsymbol{\kappa}$	Characteristic Acceleration
$\boldsymbol{l}$	Sun-to-Spacecraft Unit-Vector
ω_s	Angular Rate of Sun, Earth-Moon Rotating Frame
n	Number of Nodes
$\boldsymbol{\Delta}_i$	Defect Vector
T_i	Segment Time
ψ_i	Control Magnitude Constraint
$\boldsymbol{g}_i$	Path Constraint Vector
h_k	General Node States and/or Control Constraint
$\boldsymbol{X}$	Total Design Variable Vector
$\boldsymbol{F}$	Full Constraint Vector
$D\boldsymbol{F}$	Jacobian Matrix
ϕ	Elevation Angle from the Lunar South Pole
a	Altitude from the Lunar South Pole
δ	Sail Clock Angle
α	Sail Pitch Angle
E	Two-Body Energy with Respect to Earth
H	Two-Body Angular Momentum with Respect to Earth

*Ph.D. Candidate, School of Aeronautics and Astronautics, Purdue University, Armstrong Hall of Engineering, 701 W. Stadium Ave, West Lafayette, Indiana 47907-2045; Student Member AIAA.

†Hsu Lo Professor of Aeronautical and Astronautical Engineering, School of Aeronautics and Astronautics, Purdue University, Armstrong Hall of Engineering, 701 W. Stadium Ave, West Lafayette, Indiana 47907-2045; Fellow AAS; Associate Fellow AIAA.

I. Introduction

Communications satellites are an important component of long-duration autonomous surveillance and manned exploration of the lunar south pole. Generally, studies have been focused on deployment of at least two spacecraft for complete coverage. One solution approach involves constellations of primarily low-altitude, elliptically inclined lunar orbits, where the Earth gravity and lunar spherical harmonics are included as perturbations to a predominately two-body problem. By averaging, the variations in orbital eccentricity, argument of periapsis, and inclination are eliminated, resulting in the well-known frozen orbits.[1] According to Ely,[2] a lunar constellation of three spacecraft can be assembled, where two vehicles are always in view from the lunar surface for the polar regions. Additional long-term numerical simulations confirm that constant coverage can be achieved with two spacecraft in similar low-altitude, elliptically inclined lunar orbits.[3] Alternatively, the problem might be approached from a multi-body investigation of libration point orbits. For example, Grebow *et al.*[4] demonstrated that constant communications can be achieved with two spacecraft in many different combinations of Earth-Moon libration point orbits. Low-thrust transfers to these orbits were later computed by Howell and Ozimek.[5] These two approaches, namely frozen orbits and multi-body orbits, were later compared by Hamera *et al.*[6] Grebow *et al.* also proposed adapting NASA's Living with a Star (LWS) north and south Earth "pole-sitters" to the Moon, for possible south pole architectures.[4,7] Furthermore, NASA engineers are currently collaborating with the aerospace company Team Encounter and the National Oceanic and Atmospheric Administration (NOAA) to investigate the use of solar sails for constant surveillance of the atmosphere over the north and south poles of the Earth.[8] If such solar sail orbits exist near the lunar south pole, then only one spacecraft would be necessary to maintain continuous coverage.

The concept of practical solar sailing was introduced as early as the 1920's, according to the writings of the Soviet pioneer Tsiolkovsky and his colleague Tsander.[9] Following a proposal by Richard Garwin of IMB Watson Laboratory at Columbia University in 1958, who coined the term "solar sailing", more detailed studies of solar sailing ensued in the later 1950's, and the 1960's. Aided in part by mission applications envisioned by prominent science-fiction authors,[10] these studies have continued to the present. In 1976-1978, NASA initiated the first major mission design study incorporating a solar sail to rendezvous with Halley's Comet. In 1991, Robert L. Forward proposed an interesting and relevant mission concept using solar sails, not for transporting a spacecraft, but to maintain a stationary position. These "statites" would use solar radiation pressure to levitate in non-Keplerian trajectories. More specifically, Forward also proposed "polestats", i.e., statites that hover above the polar regions of the Earth.[11] Solar sails were also previously identified as one of five technological capabilities under consideration in NASA's Millennium Space Technology 9 (ST-9) mission. Proposals for ST-9 have included solar sails that produce thrust on the order of 0.58 mm/s^2 to values as high as 1.70 mm/s^2.[12] Assuming the latest levels of thrust acceleration available, the question remains: Can a solar sailing spacecraft employ a non-Keplerian orbit to achieve continuous line-of-sight with the lunar south pole? This feasibility study is an attempt to answer this question, and further, to develop a systematic and general method for computing these trajectories.

Trajectory design in the lunar south pole coverage problem requires a procedure for determining the orientation of the solar sail at every point in time to meet the mission objectives. Even the baseline dynamical model, that is, the Earth-Moon Restricted Three-Body Problem (RTBP), adds complexity since a closed-form solution is not available. Insight is gained by generating analytical solutions through linearization of the dynamics in the vicinity of the L_1 and L_2 libration points and exploitation of simplifying assumptions on the control, such as a constant sail orientation. The results of such an approach are limited, however, because linearized periodic orbits require stationkeeping propellant or additional sail logic to follow the reference trajectory in the nonlinear model.[13] A constant orientation of the sail also renders only a subset of the possible solutions, and eliminates potentially superior trajectories from consideration. Alternatively, if the control is allowed to vary freely, a scheme must then be identified to search for a control history that generates the desired coverage orbits. The RTBP might be exploited to generate an instantaneous equilibrium surface, with a varying solar sail orientation. Such a surface changes shape over time in the Earth-Moon system due to the changing position of the Sun.[14,15] Similar difficulties may be encountered, however, in constructing a continuous trajectory that moves along the changing equilibrium surface. Optimal control theory is another possibility for obtaining an algebraic control law, but the trajectories for lunar south pole coverage are not

easily defined by a single scalar performance index. In this preliminary design phase, the problem constraints and design objectives continue to change for different desired trajectories. The necessity to analytically re-derive and solve a complex two-point boundary value problem for continually changing objectives is a very large obstacle with this approach. In terms of numerical implementation, the lack of an algebraic control law *a priori* implies that any method for computing trajectories in the nonlinear RTPB with explicit integration is limited unless the control is estimated by some function. Additionally, the convergence radius for shooting methods using explicit integration will suffer due to long integration times.

Perhaps the best means to establish a control history in the solar sail problem, is to employ a collocation scheme.[16] These schemes are so named because the solution is a piecewise continuous polynomial that collocates, i.e., satisfies the equations of motion at discrete points. Collocation schemes can be applied with or without optimizing a performance index. In contrast to other methods, no *a priori* information on the control structure is required. A collocation scheme can easily incorporate path constraints, a step that is more difficult for explicit integration schemes. A wider convergence radius compared to shooting methods is also expected since the sensitivity of the trajectory is distributed across many segments. Collocation methods have been thoroughly investigated for solving boundary value problems[17] and optimization problems.[18] Collocation strategies are also implemented in some capacity in software packages such as COLSYS,[19] AUTO,[20] OTIS,[21] and SOCS.[22] While early uses of these methods were heavily restricted by computing speed, a recent survey by Betts[18] indicates that schemes with up to 100,000 variables are now possible.

In this study, the collocation approaches detailed in work by Hargraves and Paris,[21] Enright and Conway,[23] and Herman[24] are applied to the solar sail problem, incorporating the realistic sail thrust magnitudes from ST-9. Procedures for solving the problem with Hermite-Simpson and seventh-degree Gauss-Lobatto quadrature rules are discussed. Computational efficiency is increased by considering the sparse structure of the Jacobian matrix, enabling problems to be solved with over $100,000$ design variables. The collocation strategies are well-suited for the lunar south pole coverage problem. The proper constraints for computing periodic orbits in the Earth-Moon RTBP are introduced, and path constraints such as elevation angle and altitude relative to the lunar south pole are presented. The seventh-degree Gauss-Lobatto scheme from Herman is adapted to compute many different periodic orbits that are favorable for lunar south pole coverage. A nearby solution with smooth control is then computed using Newton's method to meet the desired constraints. The solution procedure is very robust, converging when almost no information about the initial guess is available. The schemes are also modified to transition five candidate orbits to the full model, where the actual Sun-to-spacecraft line and lunar librations are incorporated. The final trajectories from this process confirm that orbits designed in the solar sail RTBP are sufficiently accurate to be transitioned to the full model. Furthermore, most of the orbits maintain constant surveillance of the lunar south pole even in the full ephemeris model, with orbits near L_2 yielding the best coverage results. Finally, to demonstrate transfer feasibility using the sail, a steering law is presented for spiraling backwards in time from the coverage orbits to a potential geosynchronous transfer orbit. The steering law is based on evenly reducing two-body angular momentum and energy with respect to the Earth, and provides an accurate initial guess for refinement with collocation. The transfers are propellant-free, requiring only the proper alignment of the sail with the Sun, and no insertion maneuver is necessary. In total, the study demonstrates the feasibility of solar sails for constant lunar south pole coverage, and thus, further study of these mission applications is warranted.

II. System Model

A. Equations of Motion

Designing orbits for lunar south pole coverage with one spacecraft requires a simplified dynamical model before higher levels of fidelity are considered. Orbits are initially designed in the RTBP with the addition of solar sail acceleration forces. It is assumed that the Earth and the Moon move in circular orbits, and the spacecraft possesses negligible mass in comparison to the Earth and Moon. A rotating, barycentric coordinate frame is employed, with the x-axis directed from the Earth to the Moon. The z-axis is parallel to the Earth-Moon angular velocity. A solar sail provides additional acceleration $\boldsymbol{a}$ to the system. Then, the equations of motion for the system in the rotating frame are

$$\dot{\boldsymbol{x}} = \boldsymbol{f}\left(t, \boldsymbol{x}, \boldsymbol{u}\right) = \left(\begin{array}{c} \dot{\boldsymbol{r}} \\ \dot{\boldsymbol{v}} \end{array} \right) = \left\{ \begin{array}{c} \boldsymbol{v} \\ \boldsymbol{a}\left(t, \boldsymbol{u}\right) - 2\boldsymbol{\Omega} \times \boldsymbol{v} + \nabla^T U\left(\boldsymbol{r}\right) \end{array} \right\}, \tag{1}$$

where the ∇^T operator refers to the gradient-transpose. (Note that bold indicates vectors.) The components including position in the dynamical model are derivable from the potential function U,

$$U = \frac{1-\mu}{\|\boldsymbol{r}-\boldsymbol{r}_1\|} + \frac{\mu}{\|\boldsymbol{r}-\boldsymbol{r}_2\|} + \frac{1}{2}\left(x^2+y^2\right), \tag{2}$$

and x, y, and z are the components of the spacecraft's position relative to the rotating, barycentric frame. The mass parameter is μ, the Earth-Moon angular velocity is $\boldsymbol{\Omega}$, and $\boldsymbol{r}_1$ and $\boldsymbol{r}_2$ are the positions of the Earth and Moon, respectively. Equation (1) is also nondimensional, where the characteristic quantities are the total mass of the system, the distance between the Earth and Moon, and the magnitude of the system angular velocity.

For the full model, the equations of motion in the EMEJ2000 frame are

$$\dot{\boldsymbol{x}} = \boldsymbol{f}\left(t,\boldsymbol{x},\boldsymbol{u}\right) = \begin{pmatrix} \dot{\boldsymbol{R}} \\ \dot{\boldsymbol{V}} \end{pmatrix} = \left\{ \begin{array}{c} \boldsymbol{V} \\ \boldsymbol{a}\left(t,\boldsymbol{u}\right) - \mu_c \dfrac{\boldsymbol{R}}{\|\boldsymbol{R}\|^3} - \displaystyle\sum_{i=1}^{N-2} \mu_i \left(\frac{\boldsymbol{R}_i}{\|\boldsymbol{R}_i\|^3} + \frac{\boldsymbol{R}-\boldsymbol{R}_i}{\|\boldsymbol{R}-\boldsymbol{R}_i\|^3} \right) \end{array} \right\}, \tag{3}$$

where X, Y, and Z are now the spacecraft's position in the inertial frame relative the central body c. Equation (3) is also nondimensional with respect to the characteristic quantities associated with the RTBP. Note that the central body is selected to be either the Earth ($\mu_c = 1-\mu$) or the Moon ($\mu_c = \mu$), depending on the most dominant body for the current problem. An additional body, the Sun, appears in the gravity model for $N = 4$. The relative positions of the perturbing bodies are determined from the JPL DE405 ephemeris file. The magnitude of the solar radiation pressure force provided by the sail is defined as the characteristic acceleration κ, and it is directed along a unit-vector $\boldsymbol{u}$, the control parameter normal to the surface and fixed on one side of the sail. Either side of the sail may be used to provide thrust. Although the force changes when modeling the effects of a real sail, the idealized, perfectly reflective model is assumed since this study is primarily concerned with feasibility. The proper thrust direction of the two-sided sail is realized when its acceleration is modeled as

$$\boldsymbol{a} = \kappa \boldsymbol{u}\left(\boldsymbol{l}\cdot\boldsymbol{u}\right)^2 \operatorname{sgn}\left(\boldsymbol{l}\cdot\boldsymbol{u}\right), \tag{4}$$

where $\boldsymbol{l}$ is the unit-vector directed from the Sun to the spacecraft. In the model associated with the RTBP, $\boldsymbol{l}$ is simplified to rotate in a circular orbit within the Earth-Moon plane once per synodic lunar month, or with angular rate ω_s, i.e.

$$\boldsymbol{l} = \left\{\cos\left(\omega_s t\right), -\sin\left(\omega_s t\right), 0\right\}^T. \tag{5}$$

For the higher fidelity model, the actual Sun-to-spacecraft line is available from the ephemeris file. Despite the many simplifications in the RTBP model, it will be demonstrated that trajectories are still sufficiently accurate for transitioning to the full ephemeris model.

B. Natural Dynamics in the Restricted Three-Body Problem

The ability of the sail-controlled spacecraft to achieve suitable line-of-sight coverage in orbit depends on the characteristic acceleration κ. An estimate of the regions that contain feasible orbits for a given value of κ is valuable for predicting the limits of coverage capability, as well as providing an initial guess for a numerical solution. The value of $\|\nabla U\|$ offers the required sail acceleration to remain stationary in a region given only knowledge of position. Due to the symmetry and time-invariance of the restricted three-body potential, only the two-dimensional x-z projection, as it appears in figure 1, is necessary to visualize acceptable regions for orbits that yield lunar south pole coverage. For example, the contours of constant $\|\nabla U\|$ indicate that a solar sail with a $\kappa = 0.58$ mm/s^2 is restricted near the red regions that surround the collinear libration points L_1 and L_2. If a larger solar sail with $\kappa = 1.70$ mm/s^2 is available, then the feasibility region extends from L_1 and L_2 to the yellow and green locations that wrap below the lunar south pole. Given the proper corrections algorithms to adjust the trajectory, this simple visual inspection method for estimating the location for stationary points is ultimately a powerful tool that instantly bypasses the need for more complicated numerical or analytical initial guess schemes.

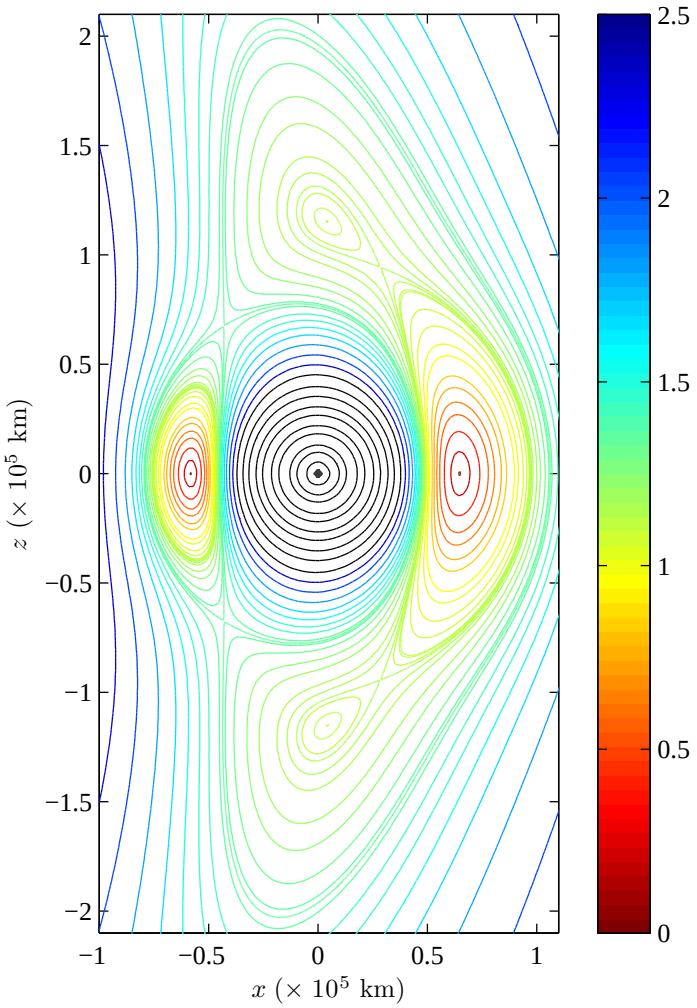

Figure 1. Contours of $\|\nabla U\|$ in mm/s^2, Moon-Centered Rotating Frame.

III. Implicit Integration

Perhaps the best method to solve this specific problem is an implicit integration scheme. By allowing most of the states and controls at points along the entire trajectory to enter the problem as unknown parameters, a numerical method is then employed to obtain a feasible trajectory. With implicit integration, no numerical integration subroutine or knowledge of a control law is required, and the sail is oriented exactly as needed at every instant to ensure that the desired trajectory is determined. An implicit integration scheme is also readily adaptable to changing mission requirements. With the increasing computational capabilities of computers and the latest advancements in linear algebra,[25] large-dimensioned problems (in this case, from long duration trajectories) are still solvable. Finally, due to the majority of the points in the trajectory entering as free variables, a more robust convergence radius is expected in comparison to other candidate methods when obtaining numerical solutions. Thus, less intuition is required even when the mission requirements may be sophisticated.

A. Collocation

With a collocation method, the infinite-dimensional problem of solving for a desired solar sail trajectory is represented by a finite set of discrete variables defined along the path. Let the trajectory be composed of n nodes, and $n-1$ total segments, where a segment is the path that connects two neighboring nodes. The set of times over all of the nodes is denoted as $\{t_1, t_2, ..., t_i, t_{i+1}, ..., t_{n-1}, t_n\}$, where t_1 is the initial time, t_n is

the final time, and the time interval for the i^{th} segment is $T_i = t_{i+1} - t_i$. In general, the system equations are a function of time, but during the numerical implementation all the segment times T_i are predetermined. It is not necessarily true, however, that each value T_i must be equal over all of the segments. Each node time t_i corresponds to a free state vector $\boldsymbol{x}_i$, and control vector $\boldsymbol{u}_i$. Using the Gauss-Lobatto quadrature rules,[26] an interpolating polynomial is constructed to ensure that the segment connecting any pair of nodes lies on a continuous trajectory. The interpolating polynomial must then satisfy system constraints known as *defects*, $\boldsymbol{\Delta}_i$.

Two independant procedures that employ polynomials with the Gauss-Lobatto quadrature rules are utilized to generate trajectories. The first technique is the well-known Hermite-Simpson method[21,23] that is equivalent to incorporating a third-degree Gauss-Lobatto integration rule of order four and yields a quadratic polynomial interpolant. A diagram of the i^{th} segment in this method appears in figure 2. Let the endpoint states and controls for the i^{th} segment, $\boldsymbol{x}_i$, $\boldsymbol{u}_i$, $\boldsymbol{x}_{i_1}$, and $\boldsymbol{u}_{i+1}$, be denoted *node points*, and the state and control at the center of the segment, $\boldsymbol{x}_{i,c}$ and $\boldsymbol{u}_{i,c}$, be labeled a *defect point*. The resulting defect point state vector is

$$\boldsymbol{x}_{i,c} = \frac{1}{2}\left(\boldsymbol{x}_i + \boldsymbol{x}_{i+1}\right) + \frac{T_i}{8}\left\{\boldsymbol{f}\left(\boldsymbol{x}_i, \boldsymbol{u}_i\right) - \boldsymbol{f}\left(\boldsymbol{x}_{i+1}, \boldsymbol{u}_{i+1}\right)\right\}. \tag{6}$$

The defect point control is computed as a linearly interpolated vector

$$\boldsymbol{u}_{i,c} = \frac{1}{2}\left(\boldsymbol{u}_i + \boldsymbol{u}_{i+1}\right). \tag{7}$$

Then, the implicit integration must satisfy

$$\boldsymbol{\Delta}_{i,c}\left(\boldsymbol{x}_i, \boldsymbol{u}_i, \boldsymbol{x}_{i+1}, \boldsymbol{u}_{i+1}\right) = \boldsymbol{x}_i - \boldsymbol{x}_{i+1} + \frac{T_i}{6}\left\{\boldsymbol{f}\left(\boldsymbol{x}_i, \boldsymbol{u}_i\right) + 4\boldsymbol{f}\left(\boldsymbol{x}_{i,c}, \boldsymbol{u}_{i,c}\right) + \boldsymbol{f}\left(\boldsymbol{x}_{i+1}, \boldsymbol{u}_{i+1}\right)\right\} = 0. \tag{8}$$

Once $\boldsymbol{x}_i$, $\boldsymbol{u}_i$, $\boldsymbol{x}_{i+1}$, and $\boldsymbol{u}_{i+1}$ are selected such that eq. (8) meets a prescribed numerical tolerance, the interpolation is an accurate approximation to the differential equations of the i^{th} segment. The third-degree,

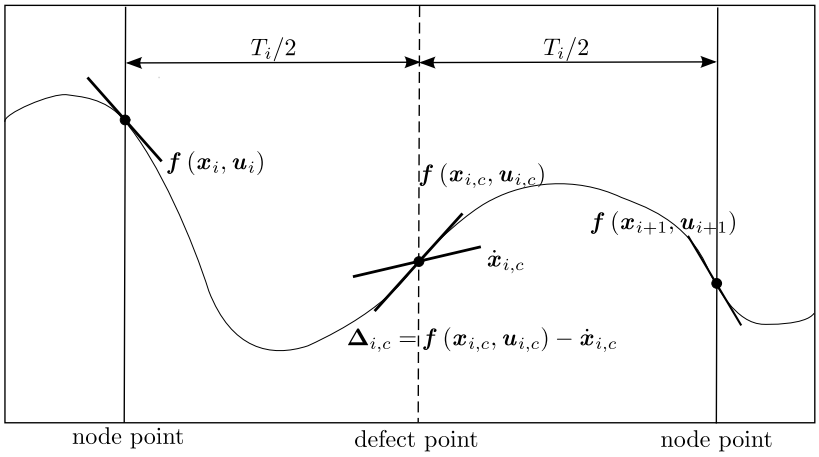

Figure 2. Illustration of Implicit Integration with the Hermite-Simpson Method.

Hermite-Simpson method is useful for fast implementation, and initial design purposes. However, the scheme suffers potential truncation error issues with a large number of nodes.[26] The procedure also requires more nodes for the same accuracy as those based on higher-order Gauss-Lobatto rules. For high-fidelity simulation, the highest possible accuracy is desired. Therefore, a seventh-degree method with an order of accuracy equal to 12, as developed by Herman,[24] is used to produce all numerical results here. For the seventh-degree method, the i^{th} trajectory segment is represented in figure 3. In addition to the node points, there are now three total defect points, $\boldsymbol{x}_{i,1}$, $\boldsymbol{u}_{i,1}$, $\boldsymbol{x}_{i,c}$, $\boldsymbol{u}_{i,c}$, $\boldsymbol{x}_{i,4}$, and $\boldsymbol{u}_{i,4}$. There are also two *internal points*, $\boldsymbol{x}_{i,2}$, $\boldsymbol{u}_{i,2}$, $\boldsymbol{x}_{i,3}$, and $\boldsymbol{u}_{i,3}$, at which the state vectors are allowed to vary, but several options are available to specify the value of the controls.[21,26,27] In this study, all of the defect point and internal point controls are linearly interpolated from the node point controls for a given segment to allow for a smoother control history as well as computational efficiency. Since there are three defect points, there are now three corresponding defects,

i.e.

$$\begin{aligned} \boldsymbol{\Delta}_{i,1}\left(\boldsymbol{x}_i, \boldsymbol{u_i}, \boldsymbol{x}_{i,2}, \boldsymbol{x}_{i,3}, \boldsymbol{x}_{i+1}, \boldsymbol{u}_{i+1}\right) &= 0, \\ \boldsymbol{\Delta}_{i,c}\left(\boldsymbol{x}_i, \boldsymbol{u_i}, \boldsymbol{x}_{i,2}, \boldsymbol{x}_{i,3}, \boldsymbol{x}_{i+1}, \boldsymbol{u}_{i+1}\right) &= 0, \\ \boldsymbol{\Delta}_{i,4}\left(\boldsymbol{x}_i, \boldsymbol{u_i}, \boldsymbol{x}_{i,2}, \boldsymbol{x}_{i,3}, \boldsymbol{x}_{i+1}, \boldsymbol{u}_{i+1}\right) &= 0. \end{aligned} \tag{9}$$

The full expressions for the seventh-degree defect states and the defects in eq. (9) are long and require several coefficients. (See Herman.[24]) All of the coefficients, however, are constants and only computed once. For numerical considerations, they are stored in a table for speed and efficiency. The third-degree and seventh-degree methods will hereafter be identified strictly as "Hermite-Simpson" and "Gauss-Lobatto," respectively, for brevity.

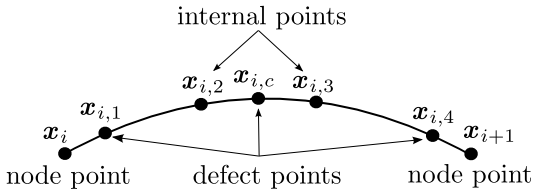

Figure 3. The Seventh-Degree Gauss-Lobatto Trajectory Segment.

B. Constraints Versus Free-Variables

To compute a continuous solution using the Hermite-Simpson method, the defects $\boldsymbol{\Delta}_{i,c}$ for each segment must be reduced to zero. This step is accomplished by allowing $\boldsymbol{x}_i$ and $\boldsymbol{u}_i$ to vary at every node point. Currently, there are $6n-6$ constraint equations and $9n$ free variables for n nodes. Recall that to implement the Gauss-Lobatto method, three defects $\boldsymbol{\Delta}_{i,1}$, $\boldsymbol{\Delta}_{i,c}$, and $\boldsymbol{\Delta}_{i,4}$, for every segment must be reduced to zero. The internal collocation points $\boldsymbol{x}_{i,2}$ and $\boldsymbol{x}_{i,3}$ are also specified as free parameters. Therefore, for the Gauss-Lobatto scheme, there are currently a total of $18n-12$ constraint equations and $21n-12$ free variables for n nodes.

For the solar sail problem, it is necessary to apply additional constraints. For example, $\boldsymbol{u}_i$ as indicated in eq. (4) must possess unit magnitude. This requirement is enforced by adding n additional constraints

$$\psi_i\left(\boldsymbol{u}_i\right) = \|\boldsymbol{u}_i\| - 1 = 0, \quad \text{for } i = 1, 2, .., n. \tag{10}$$

Additional inequality *path constraints* are also easily included in the collocation schemes. These constraints are useful in bounding the entire solution to a particular region of the phase space. The path constraints for the Hermite-Simpson method are of the form $\tilde{\boldsymbol{g}}_i\left(\boldsymbol{x}_i, \boldsymbol{u}_i\right) < 0$, where $\tilde{\boldsymbol{g}}_i$ is a m-element column vector. The constraints are converted to the product of nm equality constraints by introducing nm slack variables, i.e.

$$\boldsymbol{g}_i\left(\boldsymbol{x}_i, \boldsymbol{u}_i, \boldsymbol{\eta}_i\right) = \tilde{\boldsymbol{g}}_i\left(\boldsymbol{x}_i, \boldsymbol{u}_i\right) + \boldsymbol{\eta}_i^2 = 0, \quad \text{for } i = 1, 2, .., n, \tag{11}$$

where $\boldsymbol{\eta}_i^2$ is a vector, i.e., the element-wise square of the m-element slack variable $\boldsymbol{\eta}_i$, and of the same dimension. Thus, for the Gauss-Lobatto formulation, there are $m\left(3n-2\right)$ path constraints. The first $m\left(3n-1\right)$ constraints are

$$\begin{aligned} \boldsymbol{g}_i\left(\boldsymbol{x}_i, \boldsymbol{u}_i, \boldsymbol{\eta}_i\right) &= \tilde{\boldsymbol{g}}_i\left(\boldsymbol{x}_i, \boldsymbol{u}_i\right) + \boldsymbol{\eta}_i^2 &= 0, \\ \boldsymbol{g}_{i,2}\left(\boldsymbol{x}_{i,2}, \boldsymbol{\eta}_{i,2}\right) &= \tilde{\boldsymbol{g}}_{i,2}\left(\boldsymbol{x}_{i2}\right) + \boldsymbol{\eta}_{i,2}^2 &= 0, \quad \text{for } i = 1, 2, .., n-1. \\ \boldsymbol{g}_{i,3}\left(\boldsymbol{x}_{i,3}, \boldsymbol{\eta}_{i,3}\right) &= \tilde{\boldsymbol{g}}_{i,3}\left(\boldsymbol{x}_{i3}\right) + \boldsymbol{\eta}_{i,3}^2 &= 0, \end{aligned} \tag{12}$$

The final m constraints (the constraints for the n^{th} node) are given by eq. (11). Finally, for either the Hermite-Simpson or Gauss-Lobatto scheme, it is sometimes useful to constrain specific node states and/or control. The general form for these constraints is

$$h_k = 0, \quad \text{for } k = 1, 2, .., l. \tag{13}$$

In contrast to the constraints in eqs. (11)-(12), the constraints in eq. (10) and eq. (13) are scalar-valued.

In summary, for the Hermite-Simpson approach there are a total of $n\,(m+9)$ free parameters: $6n$ associated with the node states, $3n$ associated with the node controls, and nm for the slack variables. All the free parameters are specified in the total design variable vector $\boldsymbol{X}$, where

$$\boldsymbol{X}^T = \left(\boldsymbol{x}_1^T, \boldsymbol{u}_1^T, \boldsymbol{x}_2^T, \boldsymbol{u}_2^T, ..., \boldsymbol{x}_n^T, \boldsymbol{u}_n^T, \boldsymbol{\eta}_1^T, \boldsymbol{\eta}_2^T, ..., \boldsymbol{\eta}_n^T\right). \tag{14}$$

Additionally, there are a total of $n\,(m+7)+l-6$ constraints: $6n-6$ for the defects, n for the node controls, nm for the path constraints, and l for any additional node constraints. Together the constraints comprise the full constraint vector $\boldsymbol{F}$, i.e.

$$\boldsymbol{F}\left(\boldsymbol{X}\right)^T = \left(\boldsymbol{\Delta}_{1,c}^T, \boldsymbol{\Delta}_{2,c}^T, ..., \boldsymbol{\Delta}_{n-1,c}^T, \psi_1, \psi_2, ..., \psi_n, \boldsymbol{g}_1^T, \boldsymbol{g}_2^T, ..., \boldsymbol{g}_n^T, h_1, h_2, ..., h_l\right) = 0, \tag{15}$$

where $\boldsymbol{F}\left(\boldsymbol{X}\right)^T$ denotes the transpose of $\boldsymbol{F}$. For the Gauss-Lobatto scheme there are a total of $21n + m\,(3n-2) - 12$ free parameters: $6n$ associated with the node states, $3n$ associated with the node controls, $12n-12$ associated with the states at the internal points, and $m\,(3n-2)$ for all the slack variables. Therefore, for the Gauss-Lobatto method, $\boldsymbol{X}$ is defined as

$$\boldsymbol{X}^T = \left(\boldsymbol{x}_1^T, \boldsymbol{u}_1^T, \boldsymbol{x}_{1,2}^T, \boldsymbol{x}_{1,3}^T, \boldsymbol{x}_2^T, \boldsymbol{u}_2^T, \boldsymbol{x}_{2,2}^T, \boldsymbol{x}_{2,3}^T, ..., \boldsymbol{x}_n^T, \boldsymbol{u}_n^T, \boldsymbol{\eta}_1^T, \boldsymbol{\eta}_{1,2}^T, \boldsymbol{\eta}_{1,3}^T, \boldsymbol{\eta}_2^T, \boldsymbol{\eta}_{2,2}^T, \boldsymbol{\eta}_{2,3}^T, ..., \boldsymbol{\eta}_n^T\right). \tag{16}$$

There are also a total of $19n + m\,(3n-2) + l - 18$ constraints: $18n-18$ for the defects, n for the node controls, $m\,(3n-2)$ for the path constraints, and l for additional node constraints. The full constraint vector is

$$\begin{aligned}\boldsymbol{F}\left(\boldsymbol{X}\right)^T = \big(&\boldsymbol{\Delta}_{1,1}^T, \boldsymbol{\Delta}_{1,c}^T, \boldsymbol{\Delta}_{1,4}^T, \boldsymbol{\Delta}_{2,1}^T, \boldsymbol{\Delta}_{2,c}^T, \boldsymbol{\Delta}_{2,4}^T, ..., \boldsymbol{\Delta}_{n-1,1}^T, \boldsymbol{\Delta}_{n-1,c}^T, \boldsymbol{\Delta}_{n-1,4}^T,\\ &\psi_1, \psi_2, ..., \psi_n, \boldsymbol{g}_1^T, \boldsymbol{g}_{1,2}^T, \boldsymbol{g}_{1,3}^T, \boldsymbol{g}_2^T, \boldsymbol{g}_{2,2}^T, \boldsymbol{g}_{2,3}^T, ..., \boldsymbol{g}_n^T, h_1, h_2, ..., h_l\big) = 0.\end{aligned} \tag{17}$$

Then, for either the Hermite-Simpson or the Gauss-Lobatto procedures, the goal is to determine a nearby solution $\boldsymbol{X}^*$ that satisfies the constraint $\boldsymbol{F}\left(\boldsymbol{X}^*\right) = 0$.

C. A Nearby Solution and Newton's Method

A solution $\boldsymbol{X}_{j+1}$ such that $\|\boldsymbol{F}\left(\boldsymbol{X}_{j+1}\right)\| < \|\boldsymbol{F}\left(\boldsymbol{X}_j\right)\|$ is available by solving for $\boldsymbol{X}_{j+1}$ in

$$\boldsymbol{F}\left(\boldsymbol{X}_j\right) = D\boldsymbol{F}\left(\boldsymbol{X}_j\right) \cdot \left(\boldsymbol{X}_j - \boldsymbol{X}_{j+1}\right). \tag{18}$$

Both the Hermite-Simpson and the Gauss-Lobatto methods include exactly $2n-l+6$ more free variables than controls, and therefore $D\boldsymbol{F}\left(\boldsymbol{X}_j\right)$ in eq. (18) is a non-square matrix. As a consequence, there are generally an infinite number of solutions $\boldsymbol{X}_{j+1}$ that satisfy eq. (18). A unique solution $\boldsymbol{X}_{j+1}$ is determined by computing the $\boldsymbol{X}_{j+1}$ closest to $\boldsymbol{X}_j$, or the minimum-norm solution. In this case, $\boldsymbol{X}_{j+1}$ is

$$\boldsymbol{X}_{j+1} = \boldsymbol{X}_j - D\boldsymbol{F}\left(\boldsymbol{X}_j\right)^T \left[D\boldsymbol{F}\left(\boldsymbol{X}_j\right) \cdot D\boldsymbol{F}\left(\boldsymbol{X}_j\right)^T\right]^{-1} \boldsymbol{F}\left(\boldsymbol{X}_j\right). \tag{19}$$

The variable vector $\boldsymbol{X}_{j+1}$ is updated iteratively using eq. (19) until $\|\boldsymbol{F}\left(\boldsymbol{X}_{j+1}\right)\|$ is satisfied within a user-defined tolerance. The process converges quadratically to the nearby solution $\boldsymbol{X}^* = \boldsymbol{X}_{j+1}$.

In general, the Jacobian matrix $D\boldsymbol{F}$ is very large and sparse. The general form of $D\boldsymbol{F}$ for the Gauss-Lobatto method and $l = 0$ appears in the Appendix. Consider a problem with only 100 nodes where $\boldsymbol{g}_i$ in eq. (11) is scalar-valued, i.e., $m = 1$. For the Hermite-Simpson scheme, the length of the design variable vector $\boldsymbol{X}$ is 1,000. If there are no other node constraints ($l = 0$), the length of the corresponding constraint vector $\boldsymbol{F}$ is 794. Then the size of $D\boldsymbol{F}$ is $794 \times 1,000$. In solving the same problem with the Gauss-Lobatto method, the lengths of $\boldsymbol{X}$ and $\boldsymbol{F}$ are 2,386 and 2,180, respectively. Therefore, in this case $D\boldsymbol{F}$ is a $2,180 \times 2,386$ matrix. Due to the large number of design variables, it is apparent that even these relatively smaller problems (where $n = 100$, $m = 1$, and $l = 0$) require efficient methods for the implementation of eq. (19). The efficiency of the computation is increased by utilizing the sparseness of $D\boldsymbol{F}$. Recall from eq. (8) that for the Hermite-Simpson scheme, $\boldsymbol{\Delta}_{i,c}$ depends only on the adjacent node states and controls, and is independent of all the other node states and controls and also any other variables that appear in eq. (14). As a result, $D\boldsymbol{F}$ is primarily a block diagonal matrix of non-zero sub-matrices $D\boldsymbol{\Delta}_{i,c}$. The sparsity of $D\boldsymbol{F}$ is even more apparent when considering $D\psi_i$, $D\boldsymbol{g}_i$, and Dh_k, all of which only depend on specific node states and/or controls. In fact, for

the Hermite-Simpson scheme, there cannot be more than $n\,(18m+9l+111)-108$ non-zero entries in $D\boldsymbol{F}$. This implies that for the case when $n=100$, $m=1$, and $l=0$ (recall $D\boldsymbol{F}$ is then a $794\times 1{,}000$ matrix), there exist no more than 12,792 non-zero entries, which is about 1.61% of the total number of entries in $D\boldsymbol{F}$. Alternatively, for the Gauss-Lobatto method, there must be less than $n\,(60m+30l+543)-24m-12l-540$ non-zero entries. Then, for the case where $n=100$, $m=1$, and $l=0$, less than 1.15% of the entries are non-zero.

There are a number of ways to exploit the sparsity to increase efficiency. First, when pre-allocating the size of $D\boldsymbol{F}$, memory is only allocated for the maximum number of non-zero entries, and not for all of the zero entries (which can be *very* large). Also, considering the sparsity of $D\boldsymbol{F}$, perhaps the most efficient means of computing $\left[D\boldsymbol{F}\cdot D\boldsymbol{F}^T\right]^{-1}\boldsymbol{F}$ is to implement the Unsymmetric Multifrontal Method. The standard package UMFPACK is commonly used and appears in MATLAB®.[25] Finally, to avoid the cost of computing derivatives numerically, the non-zero elements in $D\boldsymbol{F}$ are computed analytically whenever tractable. For example, $D\psi_i$, $D\boldsymbol{g}_i$, $D\boldsymbol{g}_{i,2}$, $D\boldsymbol{g}_{i,3}$, and Dh_k are all computed analytically, and their expressions are, in general, straightforward. Unfortunately, the derivatives $D\boldsymbol{\Delta}_i$ may be quite complicated. In fact, for the Gauss-Lobatto approach, the expressions for $\boldsymbol{\Delta_i}$ are already very involved, and it is difficult to compute $D\boldsymbol{\Delta}_i$ analytically. In these cases, a numerical scheme may be more tractable. Consider computing the 6×18 sub-matrix $D\boldsymbol{\Delta}_{i,c}$ for the Hermite-Simpson method. If $\boldsymbol{x}_i=\left(x_i^{(1)},x_i^{(2)},x_i^{(3)},x_i^{(4)},x_i^{(5)},x_i^{(6)}\right)^T$ and $\boldsymbol{u}_i=\left(u_i^{(1)},u_i^{(2)},u_i^{(3)}\right)^T$, then

$$D\boldsymbol{\Delta}_{i,c}=\left\{\frac{\partial\boldsymbol{\Delta}_{i,c}}{\partial\boldsymbol{x}_i}\;\frac{\partial\boldsymbol{\Delta}_{i,c}}{\partial\boldsymbol{u}_i}\;\frac{\partial\boldsymbol{\Delta}_{i,c}}{\partial\boldsymbol{x}_{i+1}}\;\frac{\partial\boldsymbol{\Delta}_{i,c}}{\partial\boldsymbol{u}_{i+1}}\right\}, \tag{20}$$

where

$$\begin{aligned}
\frac{\partial\boldsymbol{\Delta}_{i,c}}{\partial x_i^{(j)}}&=\frac{\text{Imag}\left\{\boldsymbol{\Delta}_{i,c}\left(x_i^{(j)}+\epsilon\sqrt{-1}\right)\right\}}{\epsilon}, & \frac{\partial\boldsymbol{\Delta}_{i,c}}{\partial u_i^{(j)}}&=\frac{\text{Imag}\left\{\boldsymbol{\Delta}_{i,c}\left(u_i^{(j)}+\epsilon\sqrt{-1}\right)\right\}}{\epsilon},\\
\frac{\partial\boldsymbol{\Delta}_{i,c}}{\partial x_{i+1}^{(j)}}&=\frac{\text{Imag}\left\{\boldsymbol{\Delta}_{i,c}\left(x_{i+1}^{(j)}+\epsilon\sqrt{-1}\right)\right\}}{\epsilon}, & \frac{\partial\boldsymbol{\Delta}_{i,c}}{\partial u_{i+1}^{(j)}}&=\frac{\text{Imag}\left\{\boldsymbol{\Delta}_{i,c}\left(u_{i+1}^{(j)}+\epsilon\sqrt{-1}\right)\right\}}{\epsilon},
\end{aligned} \tag{21}$$

and ϵ is a small step-size. Therefore, all the columns of $D\boldsymbol{\Delta}_{i,c}$ in eq. (20) can be computed using eqs. (21). Similar schemes can be constructed for computing the 6×30 sub-matrices $D\boldsymbol{\Delta}_{i,1}$, $D\boldsymbol{\Delta}_{i,c}$, and $D\boldsymbol{\Delta}_{i,4}$ necessary for the Gauss-Lobatto scheme. Note that eqs. (21) are only numerical approximations of the actual partial derivatives $\frac{\partial\boldsymbol{\Delta}_{i,c}}{\partial x_i^{(j)}}$, $\frac{\partial\boldsymbol{\Delta}_{i,c}}{\partial u_i^{(j)}}$, $\frac{\partial\boldsymbol{\Delta}_{i,c}}{\partial x_{i+1}^{(j)}}$, and $\frac{\partial\boldsymbol{\Delta}_{i,c}}{\partial u_{i+1}^{(j)}}$. However, the expressions are written as equalities in eqs. (21) because, while they are only approximations, the full advantages of double-precision accuracy are exploited. Furthermore, unlike alternative finite-differencing schemes (most of which are only accurate up to single-precision just for first derivative information), it is not necessary to determine an optimal value for ϵ. The total error in the numerical scheme asymptotically approaches the round-off error as ϵ goes to zero.[28]

IV. Periodic Orbits in the Earth-Moon Restricted Three-Body Problem

Locating periodic or quasi-periodic orbits is an essential part of any long-duration mission design process. For these types of orbits, the complexity of the problem is reduced by searching for feasible solutions that are simply-periodic. Then, due to their ergodic behavior, the solutions are preserved for all time. For a solar sail in the RTBP, periodic orbits occur at periods commensurate with the lunar synodic month. For this study, only orbits with periods equal to one lunar synodic month are investigated. The periodic orbits are not embedded in families since solutions for the controlled sail are not unique. As a consequence, this study is primarily an investigation of suitable point-solutions for several orbits that support lunar south pole coverage. The general periodicity constraints are introduced, and path constraints amenable for lunar south pole coverage are derived. The method is very robust, converging on periodic solutions when almost no information about the initial guess (besides feasibility) is known. Finally, the process is employed to compute many point-solutions, however, five near-optimal solutions for lunar south pole coverage are presented.

A. Periodicity and Path Constraints

Periodic orbits are determined with periods equal to one lunar synodic month, or period $P = 29.64$ days. For the orbits in this investigation, the magnitude of the gravity gradient experienced by the spacecraft remains relatively constant. Therefore, during implementation of the collocation schemes for these orbits, a fixed value of T_i is adequate for a given number of nodes n. Then, let $T_i = P/(n-1)$. For a periodic orbit, the initial state and control must equal the final state and control, or

$$\begin{aligned} h_1(x_1, x_n) &= x_n - x_1 = 0, \quad & h_2(y_1, y_n) &= y_n - y_1 = 0, \quad & h_3(z_1, z_n) &= z_n - z_1 = 0, \\ h_4(\dot{x}_1, \dot{x}_n) &= \dot{x}_n - \dot{x}_1 = 0, \quad & h_5(\dot{y}_1, \dot{y}_n) &= \dot{y}_n - \dot{y}_1 = 0, \quad & h_6(\dot{z}_1, \dot{z}_n) &= \dot{z}_n - \dot{z}_1 = 0, \end{aligned} \tag{22}$$

$$\begin{aligned} h_7\left(u_1^{(1)}, u_n^{(1)}\right) &= u_n^{(1)} - u_1^{(1)} = 0, \\ h_8\left(u_1^{(2)}, u_n^{(2)}\right) &= u_n^{(2)} - u_1^{(2)} = 0, \\ h_9\left(u_1^{(3)}, u_n^{(3)}\right) &= u_n^{(3)} - u_1^{(3)} = 0, \end{aligned} \tag{23}$$

where $\boldsymbol{u}_i = \left(u_i^{(1)}, u_i^{(2)}, u_i^{(3)}\right)^T$, as previously defined. These constraints, in addition to the defect constraints and control constraints $\psi_i = 0$ in eq. (10), are the only constraints necessary for computing periodic orbits with the collocation schemes.

It is also quite useful to apply path constraints that completely confine the spacecraft to a region of phase space. For example, it may be desirable to force a solution to remain inside a pre-defined box in position space. For lunar south pole coverage, this is particularly useful when the *bounding box* is located beneath the south pole of the Moon. Let the lower and upper bounds of the bounding box be $\boldsymbol{r}_{lb} = (x_{lb}, y_{lb}, z_{lb})^T$ and $\boldsymbol{r}_{ub} = (x_{ub}, y_{ub}, z_{ub})^T$, respectively. Then the corresponding path constraints for the Hermite-Simpson method, where $m = 6$ in eq. (11), are

$$\boldsymbol{g}_i(\boldsymbol{r}_i, \boldsymbol{\eta}_i) = \begin{Bmatrix} \boldsymbol{r}_{lb} - \boldsymbol{r}_i \\ \boldsymbol{r}_i - \boldsymbol{r}_{ub} \end{Bmatrix} + \boldsymbol{\eta}_i^2 = 0, \quad \text{for } i = 1, 2, .., n. \tag{24}$$

Similar constraint equations apply for the Gauss-Lobatto scheme, i.e.

$$\begin{aligned} \boldsymbol{g}_i(\boldsymbol{r}_i, \boldsymbol{\eta}_i) &= \begin{Bmatrix} \boldsymbol{r}_{lb} - \boldsymbol{r}_i \\ \boldsymbol{r}_i - \boldsymbol{r}_{ub} \end{Bmatrix} + \boldsymbol{\eta}_i^2 = 0, \\ \boldsymbol{g}_{i,2}(\boldsymbol{r}_{i,2}, \boldsymbol{\eta}_{i,2}) &= \begin{Bmatrix} \boldsymbol{r}_{lb} - \boldsymbol{r}_{i,2} \\ \boldsymbol{r}_{i,2} - \boldsymbol{r}_{ub} \end{Bmatrix} + \boldsymbol{\eta}_{i2}^2 = 0, \quad \text{for } i = 1, 2, .., n-1, \\ \boldsymbol{g}_{i,3}(\boldsymbol{r}_{i,3}, \boldsymbol{\eta}_{i,3}) &= \begin{Bmatrix} \boldsymbol{r}_{lb} - \boldsymbol{r}_{i,3} \\ \boldsymbol{r}_{i,3} - \boldsymbol{r}_{ub} \end{Bmatrix} + \boldsymbol{\eta}_{i3}^2 = 0, \end{aligned} \tag{25}$$

where the last 6 constraints are given by eq. (24) for $i = n$. However, perhaps a more appropriate set of path constraints, specifically designed for lunar south pole coverage, are constraints on the elevation angle and altitude of the spacecraft from the lunar south pole. For example, it may be desired to maintain the spacecraft above a certain elevation angle ϕ_{lb} at all times and yet always remain below some altitude a_{ub}. Ignoring lunar librations, for the Hermite-Simpson scheme the constraints that accomplish this objective are

$$\boldsymbol{g}_i(\boldsymbol{r}_i, \boldsymbol{\eta}_i) = \begin{Bmatrix} \sin\phi_{lb} + \dfrac{z_i + R_M}{a_i} \\ a_i - a_{ub} \end{Bmatrix} + \boldsymbol{\eta}_i^2 = 0, \quad \text{for } i = 1, 2, .., n, \tag{26}$$

where $a_i = \sqrt{(x_i - 1 + \mu)^2 + y_i^2 + (z_i + R_M)^2}$ and R_M is the non-dimensional mean radius of the Moon. Similarly, these constraints for the Gauss-Lobatto scheme possess the form

$$\begin{aligned} \boldsymbol{g}_i(\boldsymbol{r}_i, \boldsymbol{\eta}_i) &= \begin{Bmatrix} \sin\phi_{lb} + \dfrac{z_i + R_M}{a_i} \\ a_i - a_{ub} \end{Bmatrix} + \boldsymbol{\eta}_i^2 = 0, \\ \boldsymbol{g}_{i,2}(\boldsymbol{r}_{i,2}, \boldsymbol{\eta}_{i,2}) &= \begin{Bmatrix} \sin\phi_{lb} + \dfrac{z_{i,2} + R_M}{a_{i,2}} \\ a_{i,2} - a_{ub} \end{Bmatrix} + \boldsymbol{\eta}_{i,2}^2 = 0, \\ \boldsymbol{g}_{i,3}(\boldsymbol{r}_{i,3}, \boldsymbol{\eta}_{i,3}) &= \begin{Bmatrix} \sin\phi_{lb} + \dfrac{z_{i,3} + R_M}{a_{i,3}} \\ a_{i,3} - a_{ub} \end{Bmatrix} + \boldsymbol{\eta}_{i,3}^2 = 0. \end{aligned} \tag{27}$$

Unlike the constraints for the bounding box, where $m = 6$, the constraints on elevation angle and altitude only require $m = 2$. The problem is now fully defined. The design variable vector $\boldsymbol{X}$ and constraint vector $\boldsymbol{F}$ can be constructed as indicated in eqs. (14)-(17).

B. Example Periodic Orbits

To compute some periodic orbits, assume that the elevation and altitude constraints are a priority. For this sample scenario, no initial guess is available for $\boldsymbol{X}$, which includes all the node states and controls, slack variables, and additional states and slack variables for internal points when $\boldsymbol{X}$ is associated with the Gauss-Lobatto scheme. However, the approach to the problem developed in this effort is very robust and only a few pieces of information are necessary to determine an initial guess that converges to periodic solutions using eq. (19). In general, the initial guess is established as follows:

1. Examine figure 1 and approximate a feasible region given a desired characteristic solar sail acceleration κ
2. Specify desirable values of ϕ_{lb} and a_{ub} that encompass this region
3. Within the bounds imposed by ϕ_{lb} and a_{ub}, select any set of feasible positions for all the position variables

It should be noted that the first two steps in the process may be interchanged. For example, another option is to first specify a region of interest with ϕ_{lb} and a_{ub} and then determine the value of κ necessary to maintain the spacecraft within this region. For application in the RTBP, the orbits are initially assumed to be stationary, therefore all the velocity variables are always initially set to zero. The initial time is also zero, i.e., $t_1 = 0$. An initial guess for the slack variables is determined by solving for $\boldsymbol{\eta}_i$ that satisfy eq. (11) and $\boldsymbol{\eta}_i$, $\boldsymbol{\eta}_{i,2}$, and $\boldsymbol{\eta}_{i,3}$ satisfying eq. (12). In the RTBP, let the clock angle δ be the angle between the projection of the sail normal unit vector $\boldsymbol{u}_i$ in the Earth-Moon plane and the vector $\boldsymbol{l}$. Then, the pitch angle α is the out-of-plane angle measured from the Earth-Moon plane to $\boldsymbol{u}_i$. (See figure 4.) Initially, for all node points,

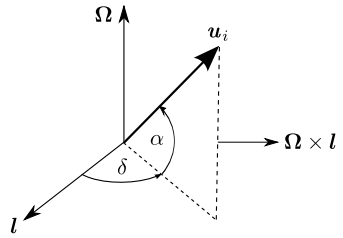

Figure 4. Relation of Control Angles to $\boldsymbol{u}_i$.

$\delta = 0°$, and $\alpha = -35.26°$ to maximize the out-of-plane component of sail thrust in the negative z direction.[13] Then the components of $\boldsymbol{u}_i$ in the rotating frame can be computed from the angles δ and α, i.e.

$$\boldsymbol{u}_i = \left\{ \begin{array}{c} \cos\alpha\cos\left(\delta - \omega_s t_i\right) \\ \cos\alpha\sin\left(\delta - \omega_s t_i\right) \\ \sin\alpha \end{array} \right\}. \tag{28}$$

Except for selecting a realistic value of κ from figure 1, very little information about the natural dynamics is necessary for computing the periodic orbits that satisfy the boundary constraints with this scheme. A control pattern is established for a solution that is close to the initial guess and meets the specified constraints. Given a feasible value of κ and an appropriate number of nodes n, the method generally determines a solution with a smooth control history in less than five iterations of eq. (19). Difficulties are only encountered when the path constraints that are selected force the spacecraft to a region that is physically impossible to maintain for the given characteristic acceleration κ, implying that, for the bounds selected, a nearby solution does not exist.

Using this strategy, many orbits favorable for lunar south pole coverage are easily computed. From all the orbits investigated, five orbits of interest are selected from three different regions. (See figure 5.) For comparison, in figure 6 the elevation angle histories for the five orbits are plotted versus time. (Hereafter the color schemes for the different orbits will remain as defined in figure 5.) Recall from figure 1, that for

the realistic sail $\kappa = 0.58$ mm/s^2, any orbits favorable for lunar south pole coverage will be located just below L_1 and L_2. Positioning the initial guess just below the L_1 and L_2 points, ϕ_{lb} is selected to be as large as physically possible for the characteristic acceleration value $\kappa = 0.58$ mm/s^2. The limiting boundary for feasible trajectories that maintain constant south pole surveillance occurs at elevation angles $\phi_{lb} = 4.2°$ for L_1 and $\phi_{lb} = 6.8°$ for L_2. A sail can reach even greater elevation angles of constant surveillance when the characteristic acceleration κ is slightly increased. For example, when $\kappa = 1.70$ mm/s^2, the limiting boundaries are $\phi_{lb} = 15.8°$ and $\phi_{lb} = 18.8°$ for L_1 and L_2, respectively. In fact, an entirely new type of orbit that appears to "hover" under the lunar south pole, is available for $\kappa = 1.70$ mm/s^2 and this trajectory can be computed from an initial guess just under the lunar south pole. The boundary of feasible solutions for this orbit is $\phi_{lb} = 15.0°$. From these results, and several other orbits investigated, it appears that for constant surveillance of the lunar south pole with a solar sail, a spacecraft near L_2 may yield the highest minimum elevation angle for both $\kappa = 0.58$ mm/s^2 and $\kappa = 1.70$ mm/s^2. Such a conclusion is consistent with figure 1, where the contours corresponding to these characteristic accelerations near L_2 extend further below the x-axis than the L_1 contours. A spacecraft in any one of these orbits also maintains constant line-of-sight with the Earth, since the solar sail orbits are displaced sufficiently far below the x-y plane. The L_2 orbits are in constant view of the far-side of the Moon as well, a feature that may be useful for future lunar missions.

The control time histories for the L_2 orbit with $\kappa = 0.58$ mm/s^2 appear in figure 7. For this study, fluctuations in the control are not constrained, but the method is general enough that they could be added. The possible off-nominal accelerations of the sail have not been modeled. Though the system allows the spacecraft to use both sides of the sail, all the orbits investigated only employ one side. For example, from figure 7 it is clear that for the L_2 orbit with $\kappa = 0.58$ mm/s^2, $-90° < \delta < 90°$. Also, since the driving factor in the investigation is ϕ_{lb}, for all computations a_{ub} is set to some arbitrarily large value. For all simulations, the Gauss-Lobatto scheme is employed with the constraints described previously and $n = 100$. This corresponds to a time-step of about 0.3 days or roughly 0.07 nondimensional time units. With the constraints implemented, the sizes of $\boldsymbol{X}$ and $\boldsymbol{F}$ are 2,684 and 2,487, respectively. Thus, over 98.6% of the entries in the matrix $D\boldsymbol{F}$ are zero.

V. Transition to Ephemeris

From a number of simplifications in the RTBP model, two critical assumptions must be further examined. First, in the RTBP the Sun-to-spacecraft line is assumed to move in the Earth-Moon plane. In reality, the Moon's orbit plane is inclined with respect to that of the Earth by about 5.15°. This difference is significant, and it is therefore necessary to demonstrate that *any* solar sail trajectory modeled in the RTBP (irrespective of the mission design objective) is sufficiently accurate for transitioning into the full ephemeris model. Second, the simplified RTBP model currently ignores lunar librations, instead assuming that the south pole of the Moon is directly below the Moon's center and stationary. In the real model, the lunar equatorial plane is inclined to Earth's orbit plane by about 1.55°. Considering these two angles, that is, the angles between the Earth orbit plane and both the lunar orbit plane and the lunar equatorial plane, it appears likely that even if the orbits can be transferred to the full model, some of the orbits from the RTBP, for example, the L_1 orbit for $\kappa = 0.58$ mm/s^2 with a minimum elevation angle of $\phi_{min} = 4.2°$, will not maintain a positive elevation angle with respect to the actual lunar south pole. However, the collocation schemes can be adapted for computations in the full model. In fact, all the orbits can be transitioned to the full model while ensuring that most do maintain a positive elevation angle ϕ_{min}.

A. Path Constraints and Control Transformation

Given multiple revolutions of any baseline orbits from the RTBP, the goal is computation of a nearby periodic solution in the full ephemeris model. The only constraints necessary for computing the nearby solution are the usual defect constraints and the control constraints $\psi_i = 0$. It is still, however, useful to enforce the path constraints that are ideal for lunar south pole coverage. To ensure that the desired elevation angles and altitudes are satisfied with respect to the actual lunar south pole, eqs. (26)-(27) must be modified. At any given time t_i, the exact position of the lunar south pole $\boldsymbol{r}_i^{sp}$ can be determined by manipulating the Euler 3-1-3 sequence for lunar librations available in the JPL DE405 ephemeris file.[3] Then for the Hermite-Simpson

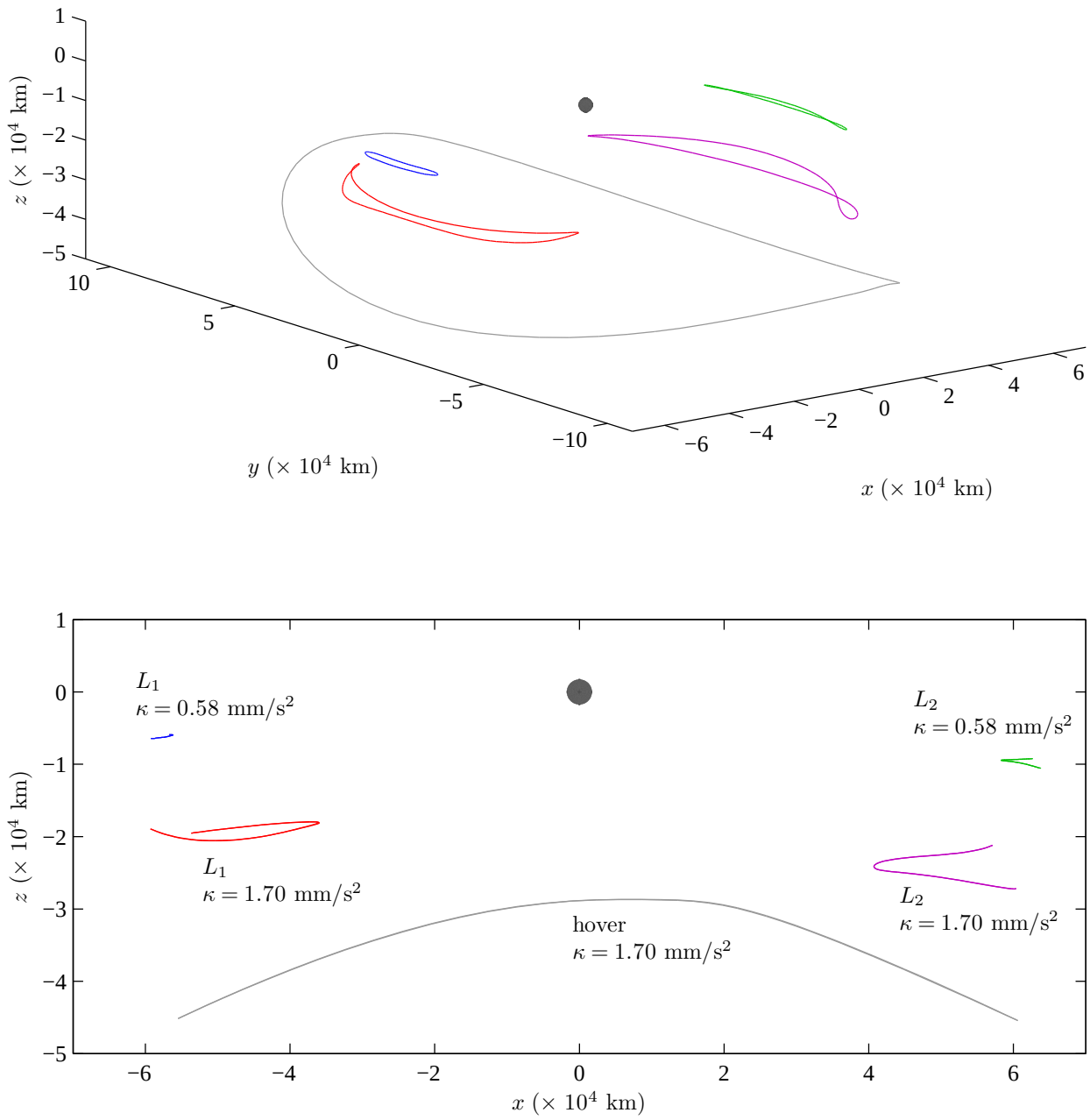

Figure 5. Periodic Orbits in the RTBP, Moon-Centered Rotating Frame (Top) and x-z Projection (Bottom).

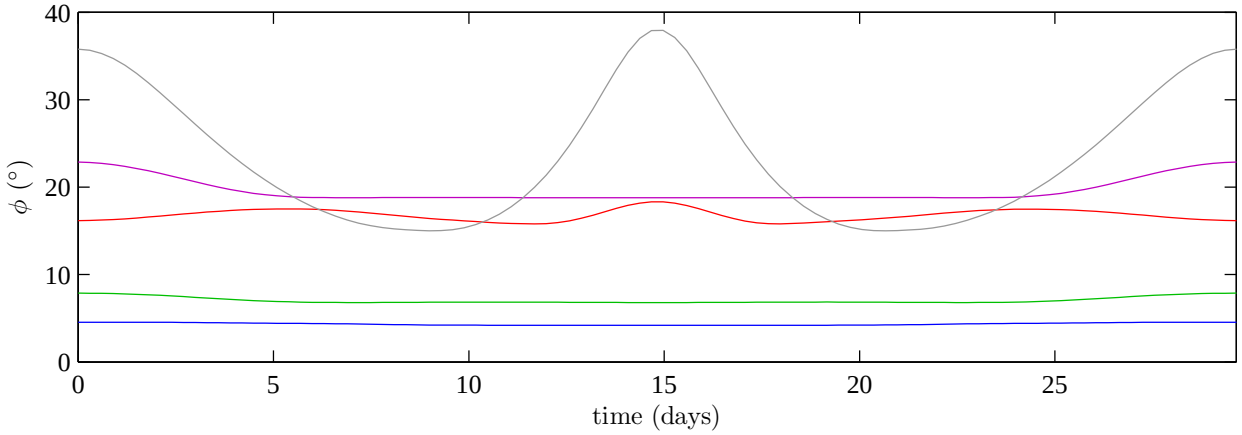

Figure 6. Elevation Angle ϕ for Periodic Orbits in the RTBP.

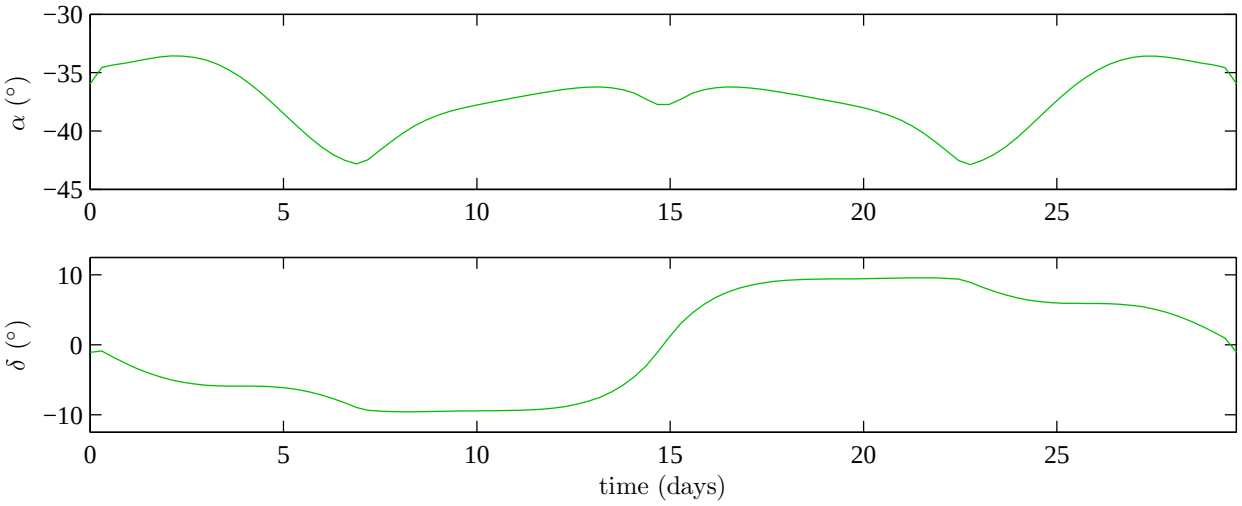

Figure 7. Control History for the L_2 Periodic Orbit in the RTBP with $\kappa = 0.58$ mm/s^2.

scheme, the path constraints for elevation angle and altitude in the full model are

$$\boldsymbol{g}_i\left(\boldsymbol{r}_i, \boldsymbol{\eta}_i\right) = \left\{ \begin{array}{c} \sin\phi_{lb} + \dfrac{\boldsymbol{r}_i^{sp} \cdot \left(\boldsymbol{r}_i^{sp} - \boldsymbol{r}_i\right)}{a_i \left\|\boldsymbol{r}_i^{sp}\right\|} \\ a_i - a_{ub} \end{array} \right\} + \boldsymbol{\eta}_i^2 = 0, \quad \text{for } i = 1, 2, .., n, \tag{29}$$

where now $a_i = \left\|\boldsymbol{r}_i - \boldsymbol{r}_i^{sp}\right\|$. Using eq. (29), similar equations can be derived for the Gauss-Lobatto scheme. Although the vector bases are now associated with the Moon-centered EMEJ2000 frame, all quantities are still nondimensional based on the characteristic quantities in the RTBP.

Before the application of a Newton iteration procedure, it is first necessary to transform all the states from the RTBP to the EMEJ2000 frame. Since the orbits are relatively close to the Moon, the Moon is set as the central body in eq. (3). The additional perturbing bodies include the Earth and the Sun, and the defects in eqs. (8)-(9) are now computed with respect to eq. (3). The controls $\boldsymbol{u}_i$ must also be adjusted to be defined relative to the real Sun-to-spacecraft line. Therefore, given $\boldsymbol{u}_i = \left(u_i^{(1)}, u_i^{(2)}, u_i^{(3)}\right)^T$ from the RTBP,

first α_i and δ_i are computed, i.e.

$$\begin{aligned} \alpha_i &= \sin^{-1} u_i^{(3)}, \\ \delta_i &= \tan^{-1}\left(\frac{u_i^{(1)}\sin\omega_s t_i + u_i^{(2)}\cos\omega_s t_i}{u_i^{(1)}\cos\omega_s t_i - u_i^{(2)}\sin\omega_s t_i}\right), \end{aligned} \tag{30}$$

where $-90^\circ \leq \sin^{-1}(\cdot) \leq 90^\circ$ and $-180^\circ \leq \tan^{-1}(\cdot) \leq 180^\circ$, and ω_s is as calculated in RTBP. Then, to determine $\boldsymbol{u}_i$ in the EMEJ2000 frame given α_i and δ_i, consider using

$$\boldsymbol{u}_i = \left[\begin{array}{ccc} \boldsymbol{l}_i & \dfrac{\boldsymbol{h}_i \times \boldsymbol{l}_i}{\|\boldsymbol{h}_i \times \boldsymbol{l}_i\|} & \boldsymbol{l}_i \times \dfrac{\boldsymbol{h}_i \times \boldsymbol{l}_i}{\|\boldsymbol{h}_i \times \boldsymbol{l}_i\|} \end{array}\right] \left\{\begin{array}{c} \cos\alpha_i \cos\delta_i \\ \cos\alpha_i \sin\delta_i \\ \sin\alpha_i \end{array}\right\}, \tag{31}$$

where both $\boldsymbol{l}_i$ and $\boldsymbol{h}_i$ possess unit magnitudes. Here the instantaneous direction of the Sun-to-spacecraft line $\boldsymbol{l}_i$ is extracted from the ephemeris files. The vector $\boldsymbol{h}_i$ is the unit vector parallel to the angular momentum associated with the Earth's orbit relative to the Sun, and is also determined from the files.

B. Results

Since the orbits are periodic in the RTBP, multiple revolutions can be quickly obtained by "stacking" the node states and controls for a baseline 25-revolution, two-year mission. The number of nodes per revolution is adjusted to 35, for a total number of nodes $n = 851$. From eqs. (4)-(5), it is apparent that an epoch must be identified when the Moon is at opposition to match the conditions at $t = 0$ for the simple RTBP model. The total lunar eclipse of 2011 December 10, 14:31:46 UTC meets this requirement and is selected as the epoch for all of the orbits. Since the segment time T_i remains fixed, all the body locations in the system model, as well as the location of the lunar south pole, are computed prior to applying the collocation scheme and stored in memory for future access. Therefore, the ephemeris files are never called during implementation of the collocation schemes. As previously stated, the node states and controls (as well as the states corresponding to the internal points for the Gauss-Lobatto scheme) are transformed into the Moon-centered EMEJ2000 frame, and the values of ϕ_{lb} and a_{ub} are selected. The values for the bounds ϕ_{lb} and a_{ub} must be such that the initial guess is feasible or at least very close to feasible. If the initial guess is infeasible, then using eqs. (11)-(12) to compute initial values for the slack variables, the variables are defined in terms of the real part. Using the transformed guess from the RTBP and the bounds described in eq. (29), eq. (19) is once again applied in an iterative manner. In just a few iterations, the scheme successfully computes quasi-periodic solutions for solar sail trajectories in the ephemeris Earth-Moon pulsating, rotating frame.

All five orbits designed in the RTBP are successfully transitioned to the full model using the Gauss-Lobatto method, and the results appear in figure 8 where the orbits are plotted in the Earth-Moon pulsating, rotating frame. For comparison, elevation angle is plotted as a function of time for both L_2 orbits in figure 9. After transition, the L_1 orbit with $\kappa = 0.58$ mm/s^2 possesses a minimum elevation angle $\phi_{min} = -2.70^\circ$, that is, "below" the horizon and out of sight of the south pole. In contrast, for this κ, the L_2 orbit is barely feasible after transitioning to the full model, where $\phi_{min} = 0.01^\circ$. Therefore, it appears that for the more realistic sail with $\kappa = 0.58$ mm/s^2, only orbits near L_2 maintain constant surveillance of the lunar south pole in the full model. For the slightly larger characteristic acceleration $\kappa = 1.70$ mm/s^2, however, all the orbits maintain positive elevation angles in the ephemeris model. The minimum elevation angles for L_1 and L_2 are $\phi_{min} = 9.10^\circ$ and $\phi_{min} = 11.91^\circ$, respectively, and $\phi_{min} = 8.20^\circ$ for the hover orbit. Due to the lunar librations, it is not surprising that nearly all the orbits lose about 6.7° of elevation between the RTBP and ephemeris models.

A sample of the control time histories for the L_2 orbit for $\kappa = 0.58$ mm/s^2 appear in figure 10. Note that upon transition to the full model, the control histories remain smooth, and are also relatively slow. (At most, only a few degrees of re-orientation are required per day.) Quasi-periodic orbits may be computed for up to 100 revolutions of the baseline orbit, and the results do not vary. Note that for 100 revolutions (approximately 8 years), $n = 3,401$, setting the size of $\boldsymbol{X}$ and $\boldsymbol{F}$ to 91,811 and 85,003, respectively. However, roughly 99.97% of the entries in the matrix $D\boldsymbol{F}$ are zero.

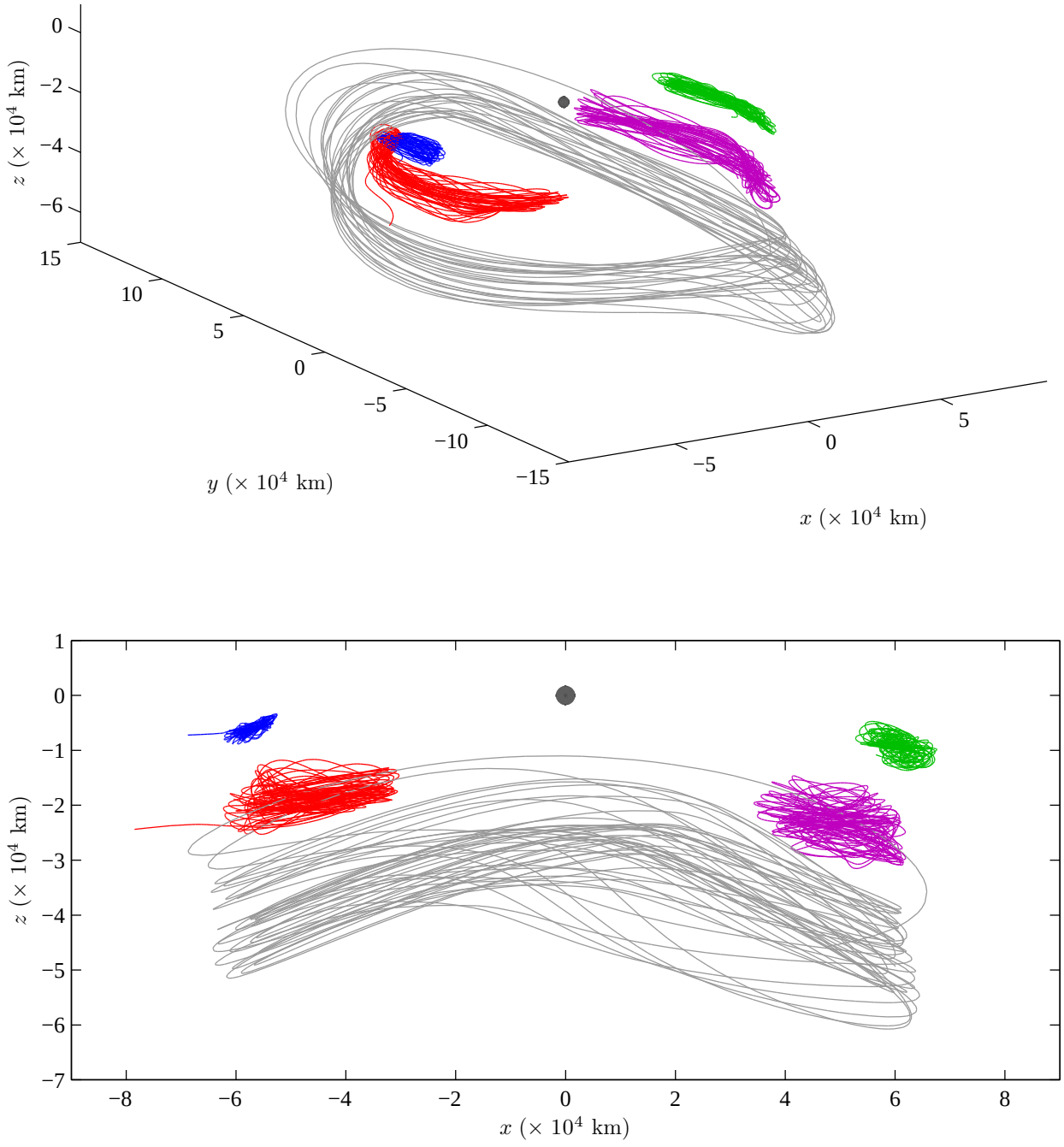

Figure 8. Quasi-Periodic Orbits in the Full Ephemeris Model, Moon-Centered Pulsating, Rotating Frame (Top) and x-z Projection (Bottom).

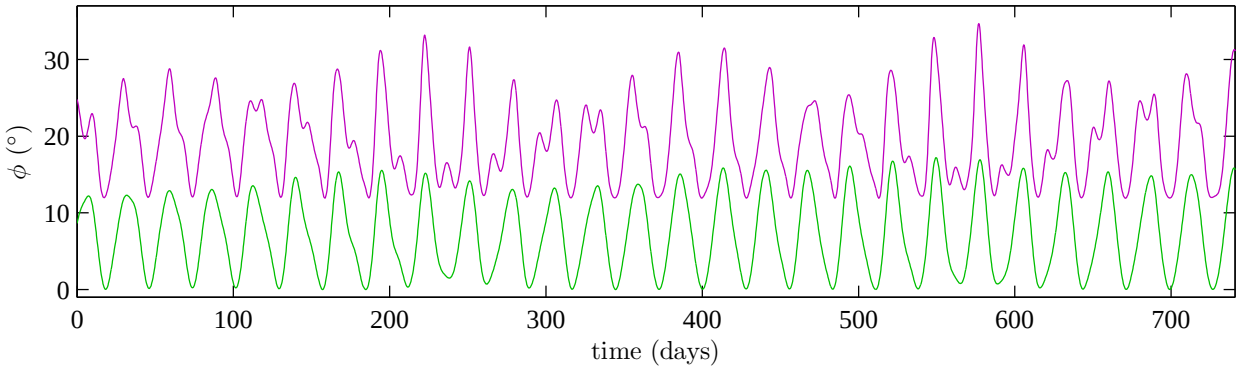

Figure 9. Elevation Angle ϕ for the L_2 Quasi-Periodic Orbits in the Full Ephemeris Model.

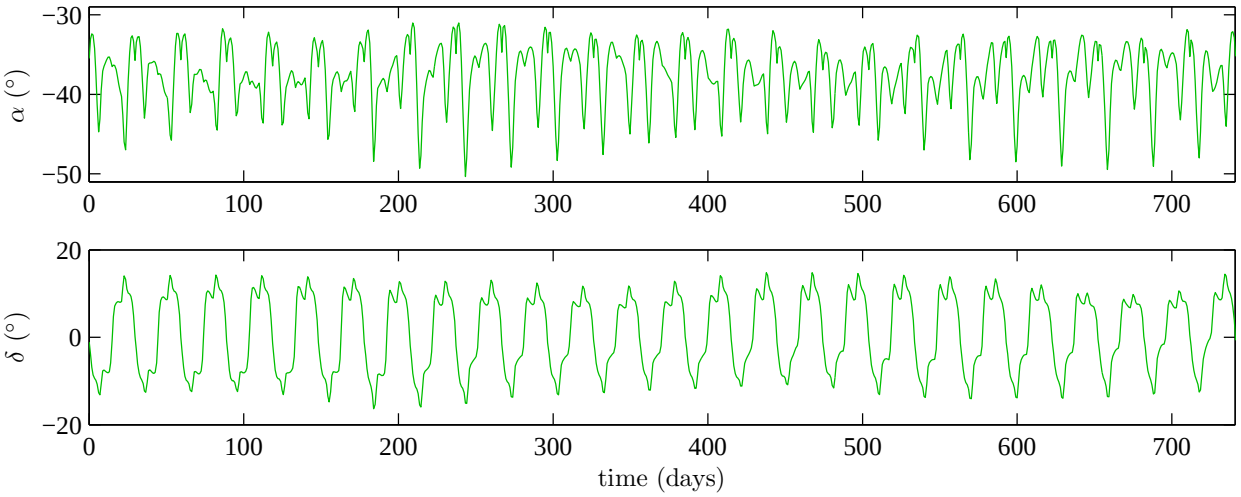

Figure 10. Control History for the L_2 Quasi-Periodic Orbit in the Full Ephemeris Model with $\kappa = 0.58$ mm/s^2.

VI. Transfer Trajectories

The use of a solar sail for lunar south pole coverage implies that the spacecraft ideally inserts into the orbit from a propellant-free transfer trajectory. (Alternative schemes are also available, but the use of propellant for thrusting is required.[5]) Although a spiral-out from low-Earth orbit is impractical due to atmospheric drag, an initial "piggy-back" leg along a geosynchronous transfer orbit (GTO) has been proposed as a viable option by previous researchers.[9] To reduce the potential effects of drag, which are not modeled in this study, periapsis for the GTO is defined as 1,000 km.

A. Backwards Integration

Due to very long flight times and sensitive, nonlinear dynamical behavior near the Earth, an accurate initial guess is required to refine a transfer trajectory with the collocation procedure. An intuitive, explicitly integrated initial guess scheme is developed by assuming a steering law for the solar sail. All integration occurs in the EMEJ2000 coordinate frame in the full ephemeris model, since the RTBP offers no major simplifying assumptions that can be exploited with this transfer scheme. Numerical integration also occurs in backwards time, allowing the initial state to be fixed on the lunar south pole coverage orbit at the proper insertion date in the ephemeris model; as a consequence, the exact GTO remains unspecified. Then, the initial guess scheme requires only that the two-body energy E and the angular momentum H with respect to the Earth, are matched as close as possible to the corresponding GTO values when the propagation terminates.

To reduce the energy during backwards numerical integration, the velocity-pointing steering law detailed in figure 11 is employed. The sail acceleration $\boldsymbol{a}$ is initially aligned along the inertial velocity vector $\boldsymbol{V}$, but when $\boldsymbol{l} \cdot \boldsymbol{V}$ is negative, the sail is oriented such that $\boldsymbol{u} \perp \boldsymbol{l}$ to produce no thrust. For a two-sided sail, $\boldsymbol{u}$ flips 180° at the completion of every cycle, and as a consequence $\boldsymbol{u}$ is either parallel or anti-parallel to $\boldsymbol{V}$ during thrusting. When the sail requires re-orientation to an attitude that yields no acceleration, i.e., the sail is "off", $\delta = \pm 90°$ and α is oriented such that $\boldsymbol{u}$ is as close as possible to $\boldsymbol{V}$ (or $-\boldsymbol{V}$ depending on the cycle) to ensure a smooth control transition the next time the sail is activated.

Using only this algorithm, E is reduced without any attention to the rate of decrease in H. Problems arise during backwards propagation because H decreases too quickly, resulting in a highly elliptical orbit that passes through the Earth. Other possible approaches, such as McInnes' locally optimal steering law,[9] reduce H even faster, since most thrusting occurs in the vicinity of apoapsis. For similar rates of decrease in E and H, the velocity-pointing steering law is, therefore, modified to force maneuvers away from apoapsis during the transfer. This modification is accomplished by selecting the Earth-relative flight-path-angle γ as an additional switching condition. Thus, the sail is now always off unless $\boldsymbol{l} \cdot \boldsymbol{V} = 0$ and γ lies within an acceptable region, at which point the sail switches on. This new "E-H" steering law corresponds to wait-times until the correct phasing of the transfer with the Sun-to-spacecraft line occurs. Details for the full implementation of this method are available by examination of the function generator in figure 12.

For numerical considerations upon transition into collocation, initial guesses that pass through the Earth are avoided. The stopping condition for the integration, that is, $E = 0$ and $H > 0$, is sufficient to ensure this behavior. Backwards integration of the E-H steering law is also repeated at initial conditions corresponding to nodes around the baseline ephemeris coverage orbit until an accurate initial guess is obtained. Since the coverage orbit is a converged ephemeris solution, a successful transfer obtained in collocation will result in a continuous insertion without a maneuver.

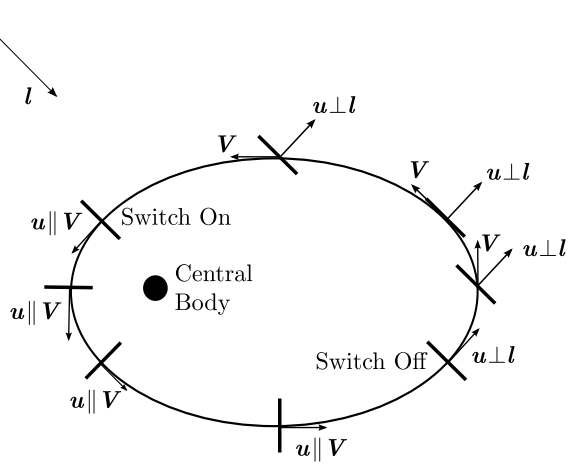

Figure 11. Velocity-Pointing Steering Law.

B. Refinement with Collocation

From an accurate initial guess obtained with the E-H thrusting law, the trajectory must be refined with collocation to generate a feasible solution. In formulating the new constraint vector (eq. (17)), the defect constraints $\boldsymbol{\Delta}_i$ (eq. (9)) and control-magnitude constraints ψ_i (eq. (10)) must be enforced as usual, but no path constraints (eq. (12)) are required, i.e. $m = 0$. The boundary conditions that bracket the transfer are enforced by adding general constraints (eq. (13)) at the 1st node and the n^{th} node. These boundary conditions are defined as the insertion state on the lunar south pole coverage orbit and the energy and

Input γ_{min} & E_{GTO}, and set $s = 1$.

DO WHILE $E < E_{GTO}$

DO WHILE $\gamma < \gamma_{min}$

Propagate eq. (3) with $\boldsymbol{a}(t, \boldsymbol{u}) = 0$ until $\boldsymbol{l} \cdot \boldsymbol{V} = 0$ & $d(\boldsymbol{l} \cdot \boldsymbol{V})/dt < 0$.

Update γ.

END

Propagate eq. (3) with $\boldsymbol{u} \parallel (s\boldsymbol{V})$ until $\boldsymbol{l} \cdot \boldsymbol{V} = 0$ & $d(\boldsymbol{l} \cdot \boldsymbol{V})/dt > 0$.

Update E, and set $s = -s$.

END

Figure 12. Function Generator for the E-H Steering Law.

angular momentum associated with GTO, i.e.

$$\begin{aligned}
h_1(X_n) &= X_n - X^*, \\
h_2(Y_n) &= Y_n - Y^*, \\
h_3(Z_n) &= Z_n - Z^*, \qquad & h_1(\boldsymbol{x}_1) &= \|\boldsymbol{V}_1\|^2/2 - (1-\mu)/\|\boldsymbol{R}_1\| - E_{GTO}, \\
h_4\left(\dot{X}_n\right) &= \dot{X}_n - X^*, \qquad & h_8(\boldsymbol{x}_1) &= \|\boldsymbol{R}_1 \times \boldsymbol{V}_1\| - H_{GTO}, \\
h_5\left(\dot{Y}_n\right) &= \dot{Y}_n - Y^*, \\
h_6\left(\dot{Z}_n\right) &= \dot{Z}_n - Z^*,
\end{aligned} \tag{32}$$

where the superscript "*" identifies a condition along the coverage orbit. Since the transfer involves a large number of spirals around the Earth, one strategy to compensate for the sensitive dynamical region is to employ an adaptive refinement in the nodal distribution.[29] However, the complications of such a process are bypassed by using pre-specified time ratios from the explicit integration of the E-H thrusting law. These time ratios are already spaced in recognition of the sensitive dynamics, and since an accurate initial guess is inputted into the procedure, there is no need for adaptive refinement. Since the time on each trajectory segment is fixed, the locations of all celestial bodies within the DE405 ephemeris file are only initialized once. The Earth is selected as the central body in eq. (3), with the Sun and Moon acting as perturbing bodies. This configuration is useful for numerical accuracy due to the many spirals that pass near the Earth. For each transfer, 5,000 nodes are selected, resulting in 104,988 free variables, 94,990 total constraints, and a $D\boldsymbol{F}$ matrix including over 99.96% zero entries. The states and controls are adjusted until a control history is determined along a continuous trajectory that satisfies the constraints in eq. (17).

A successfully converged, full ephemeris sample transfer to the L_2 orbit corresponding to $\kappa = 0.58$ mm/s^2 appears in figure 13. The total transfer time from GTO is 401 days, with 106 days of on-time, and 397 on/off switches of the sail to arrive at the orbit (shown in green). These switches can be visualized in figure 13 since the red arcs correspond to on-times and the blue phases correspond to off-times. Inspection of the control history in figure 14 reveals these switch times as the instances when $\delta = \pm 90°$. Proper phasing of the Sun, orbit, and sail is important, since the sail is only active 26% of the time. It is again emphasized that this resulting transfer requires no actual propellant, despite the fact that the transfer time appears long. Such long times are feasible for the mission concept of satellites designed for purposes of communications.

VII. Mission Design Summary

Hundreds of orbit scenarios were generated during the course of this investigation, but five orbits were specifically selected as feasible and also possessed the largest elevation angle lower bound ϕ_{lb}. Therefore, the orbits are near-optimal for purposes of lunar south pole coverage. Each scenario of interest is successfully generated in the full ephemeris model. (See table 1.) Results associated with the transfer phase and the

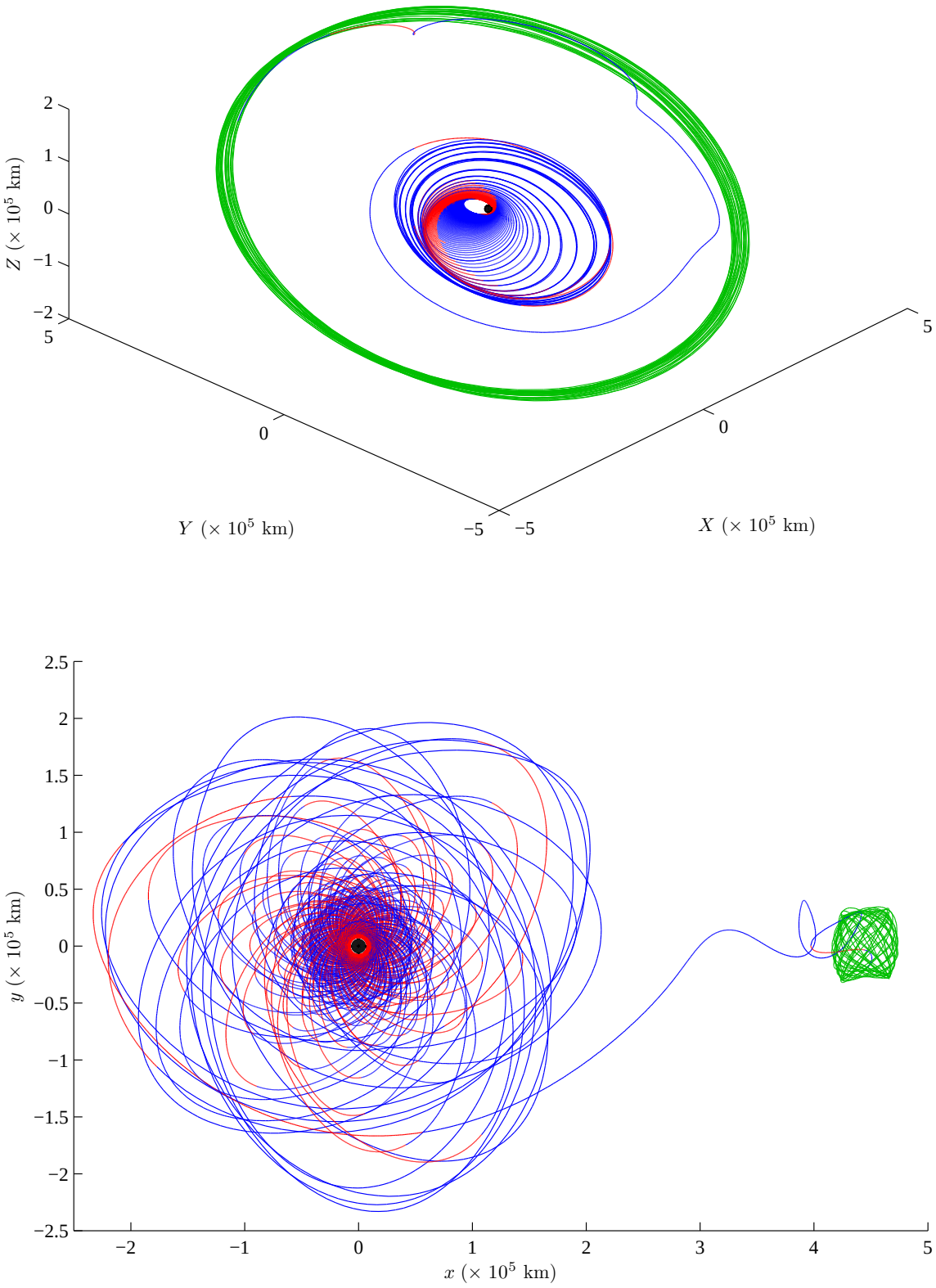

Figure 13. Transfer to the L_2, $\kappa = 0.58$ mm/s^2 Quasi-Periodic Orbit in the Full Ephemeris Model, Earth-Centered EMEJ200 Frame (Top) and x-y projection in the Earth-Centered Pulsating, Rotating Frame (Bottom).

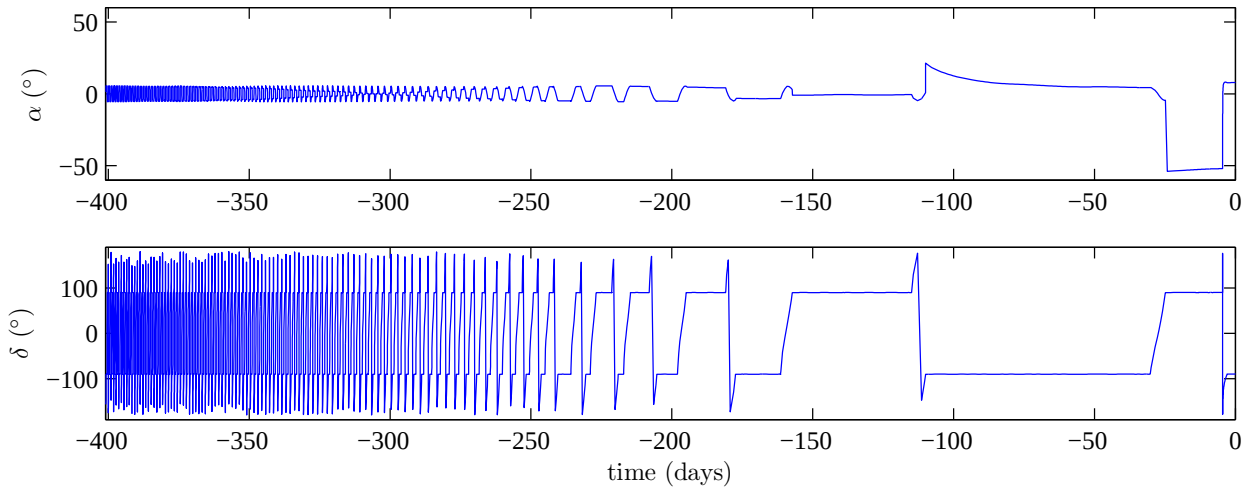

Figure 14. Control History for Transfer to the L_2, $\kappa = 0.58$ mm/s^2 Quasi-Periodic Orbit in the Full Ephemeris Model.

orbit phase are separated by the horizontal lines in the row corresponding to insertion. For the transfers, a higher percentage of sail on-time is observed in the orbits with a lower characteristic acceleration. When more thrust acceleration is available, the transfer time is not necessarily faster due to the unique phasing required in the system. As expected, the best coverage is obtained by the orbits in the vicinity of L_2. In fact, lunar librations completely eliminate the possibility for continuous line-of-sight with the lunar south pole for the set of orbits near L_1 when $\kappa = 0.58$ mm/s^2. As characteristic acceleration increases for the sails, a large increase in elevation angle is observed as a larger out-of-plane force is available. The unique "hover orbit" possesses the best maximum elevation angle, but suffers a smaller minimum elevation angle and a greater maximum altitude than the other orbits. All of the altitudes for the orbits in this study are comparable to the maximum apolune altitudes in the previous investigation by Grebow *et al.*[4] Other studies, however, indicate that these altitudes are feasible for use with existing communications hardware.[6]

VIII. Conclusions

A systematic, robust approach is developed to compute periodic orbits in the RTBP and quasi-periodic orbits in the full ephemeris model for lunar south pole coverage. The numerical process converges on solutions with very little *a priori* knowledge of the shape of these orbits or a control history. Furthermore, iteration on the largest possible minimum elevation angle reveals that the best coverage for a single spacecraft is achieved in the vicinity of the L_2 point. The implicit integration scheme that is developed to generate the orbits is adaptable to changing mission requirements, even beyond the problem of lunar south pole coverage. A transfer scheme based on simultaneously decreasing energy and angular momentum may be used in conjunction with the collocation strategy to yield feasible transfer trajectories. The collocation method successfully converges these trajectories, even when the number of design variables exceeds 100,000. The baseline transfers require no propellant and no additional insertion maneuvers are necessary. This feasibility study demonstrates that, with current technology, solar sails remain an option for continuous lunar south pole coverage with a single spacecraft. Further study of this mission application is, thus, clearly warranted.

IX. Acknowledgements

The authors thank Professor Robert Melton for suggesting the investigation of Gauss-Lobatto quadrature rules, and potential procedures for increasing computational efficiency. The authors also thank Mr. Bruce Campbell for initially suggesting research on solar sails for lunar south pole coverage. This work was carried out at Purdue University and the NASA Goddard Spaceflight Center with the Flight Dynamics Analysis Branch under the supervision of Mr. David Folta. Portions of this work were supported by the NASA

Graduate Student Researchers Program (GSRP) fellowship and the Purdue Graduate Assistance in Areas of National Need (GAANN) fellowship.

References

[1]Elipe, A., and Lara, M., "Frozen Orbits about the Moon," *Journal of Guidance, Control, and Dynamics*, Vol. 26, No. 2, 2003, pp. 238-243.

[2]Ely, T., "Stable Constellations of Frozen Elliptical Inclined Orbits," *Journal of the Astronautical Sciences*, Vol. 53, No. 3, 2005, pp. 301-316.

[3]Howell, K., Grebow, D., and Olikara, Z., "Design Using Gauss' Perturbing Equations with Applications to Lunar South Pole Coverage," Paper AAS 07-143, *17th AAS/AIAA Spaceflight Mechanics Meeting*, Sedona, Arizona, January 28-February 1, 2007.

[4]Grebow, D., Ozimek, M., and Howell, K., "Multi-Body Orbit Architectures for Lunar South Pole Coverage," *Journal of Spacecraft and Rockets*, Vol. 45, No. 2, 2008, pp. 344-358.

[5]Howell, K., and Ozimek, M., "Low-Thrust Transfers in the Earth-Moon System Including Applications to Libration Point Orbits," Paper AAS-343, *2007 AAS/AIAA Astrodynamics Specialist Conference*, Mackinac Island, Michigan, August 19-23, 2007.

[6]Hamera, K., Mosher, T., Gefreh, M., Paul, R., Slavkin L., and Trojan, J., "An Evolvable Lunar Communication and Navigation Constellation Architecture," Paper AIAA-2008-5480, *26th International Communications Satellite Systems Conference*, San Diego, California, June 10-12, 2008.

[7] "Space Science Enterprise 2000 Strategic Plan," [online publication], http://spacescience.nasa.gov/admin/pubs/strategy/2000/ [retrieved 11 December 2007].

[8]Garner, C., Price, H., Edwards, D., and Baggett, R., "Developments and Activities in Solar Sail Propulsion," Paper AIAA-2001-3234, *37th AIAA/ASME/SAE/ASEE Joint Propulsion Conference and Exhibit*, Salt Lake City, Utah, July 8-11, 2001.

[9]McInnes, C., *Solar Sailing: Technology, Dynamics and Mission Applications*, Springer-Verlag, Berlin, 1999.

[10]Clarke, A., *The Wind from the Sun*, Harcourt Brace Jovanovich, inc., New York, 1972.

[11]Forward, R., "Statite Apparatus and Method of Use," World International Property Organization, International Patent Classification B64G 1/36, International Publication Number WO 90/07450, July, 1990.

[12]Lichodzeijewski, D., and Derbes, B., "Vacuum Deployment and Testing of a 20M Solar Sail System," Paper AIAA-2006-1705, *47th AIAA/ASME/ASCE/AHS/ASC Structures, Structural Dynamics, and Materials Conference*, Newport, Rhode Island, May 1-4, 2006.

[13]McInnes, C., "Solar Sail Trajectories at the Lunar L_2 Lagrange Point," *Journal of Spacecraft and Rockets*, Vol. 30, No. 6, 1993, pp. 344-358.

[14]McInnes, C., McDonald, A., Simmons, J., and MacDonald, E.,"Solar Sail Parking in Restricted Three-Body Systems," *Journal of Guidance, Control, and Dynamics*, Vol. 17, No. 2, 1994, pp. 399-406.

[15]Wawrzyniak, G., "The Solar Sail Lunar Relay Station: An Application of Solar Sails in the Earth-Moon System," *59th IAC Congress*, Glasgow, Scotland, September 29-October 3, 2008.

[16]Melton, R., "Comparison of Direct Optimization Methods Applied to Solar Sail Problems," Paper AIAA 2002-4728, *2002 AIAA/AAS Astrodynamics Specialist Conference and Exhibit*, Monterey, California, August 5-8, 2002.

[17]Russell, R., and Shampine, L., "A Collocation Method for Boundary Value Problems," *Numerical Mathematics*, Vol. 19, 1972, pp. 1-28.

[18]Betts, J.,"Survey of Numerical Methods for Trajectory Optimization," *Journal of Guidance, Control, and Dynamics*, Vol. 21, No. 2, 1998, pp. 193-207.

[19]Ascher, U., Christiansen, J., and Russell, R., "COLSYS-A Collocation Code for Boundary-Value Problems," *Codes for Boundary Value Problems in Ordinary Differential Equations*, Vol. 76, Springer-Verlag, Berlin, 1979.

[20]Dodel, E., Paffenroth, R., Champneys, A., Fairgrieve, T., Kuznetsov, Y., Sandstede, B., and Wang, X., "AUTO2000: Continuation and Bifurcation Software for Ordinary Differential Equations," [online publication], http://personal.maths.surrey.ac [retrieved 17 July 2008], 2000.

[21]Hargraves, C., and Paris, S., "Direct Trajectory Optimization Using Nonlinear Programming and Collocation," *Journal of Guidance, Control, and Dynamics*, Vol. 10, No. 4, 1987, pp. 338-342.

[22]Betts, J., and Huffman, W., "Sparse Optimal Control Software SOCS," Boeing Information and Support Services, Mathematics and Engineering Analysis Technical Document MEA-LR-085, The Boeing Co., Seattle, Washington, July 1997.

[23]Enright, P., and Conway, B., "Optimal Finite-Thrust Spacecraft Trajectories Using Collocation and Nonlinear Programming," *Journal of Guidance, Control, and Dynamics*, Vol. 14, No. 5, 1991, pp. 981-985.

[24]Herman, A., "Improved Collocation Methods With Applications to Direct Trajectory Optimization," Ph.D. Dissertation, Department of Aerospace Engineering, University of Illinois at Urbana-Champaign, Urbana, Illinois, September 1995.

[25]Davis, T., "UMFPACK Version 4.6 User Guide," [online publication], http://www.cise.ufl.edu/research/sparse/umfpack [retrieved 18 July 2008], Department of Computer and Information Science and Engineering, University of Florida, Gainesville, Florida, 2002.

[26]Herman, A., and Conway, B., "Direct Optimization Using Collocation Based on High-Order Gauss-Lobatto Quadrature Rules," *Journal of Guidance, Control, and Dynamics*, Vol. 19, No. 3, 1996, pp. 592-599.

[27]Enright, P., "Optimal Finite-Thrust Spacecraft Trajectories Using Direct Transcription and Nonlinear Programming," Ph.D. Dissertation, Department of Aerospace Engineering, University of Illinois at Urbana-Champaign, Urbana, Illinois, January 1991.

[28]Martins, J., Kroo, I., and Alonso, J., "An Automated Method for Sensitivity Analysis using Complex Variables," Paper AIAA-2000-0689, *38th Aerospace Sciences Meeting and Exhibit*, Reno, Nevada, January 10-13, 2000.

[29]Russell, R., and Christiansen, J., "Adaptive Mesh Selection Strategies for Solving Boundary Value Problems," *SIAM Journal on Numerical Analysis*, Vol. 15, No. 1, 1978, pp. 59-80.

Table 1. Summary of Example Scenarios in the Full Ephemeris Model.

	$\kappa = 0.58$ mm/s^2		$\kappa = 1.70$ mm/s^2		
Type	L_1	L_2	L_1	L_2	hover
Epoch (UTC)	4 Feb 2011 16:48:00	8 Nov 2010 04:48:00	26 May 2011 02:24:00	17 Oct 2010 07:12:00	23 Apr 2011 16:48:00
Transfer Time (days)	309	401	199	446	248
On-Time (days)	99	106	35	34	35
% On-Time	32	26	17	8	14
No. Switches	429	397	113	113	119
Insertion Date (UTC)	10 Dec 2011 14:24:00	14 Dec 2011 02:24:00	10 Dec 2011 14:24:00	6 Jan 2012 14:24:00	27 Dec 2011 04:48:00
ϕ_{min} (°)	-2.70	0.01	9.10	11.91	8.20
ϕ_{max} (°)	12.46	17.21	27.43	34.68	45.68
ϕ_{avg} (°)	4.18	7.13	16.14	19.37	22.37
a_{min} (km)	53,000	58,000	55,500	57,000	68,500
a_{max} (km)	70,000	70,500	84,500	76,000	138,000

Appendix

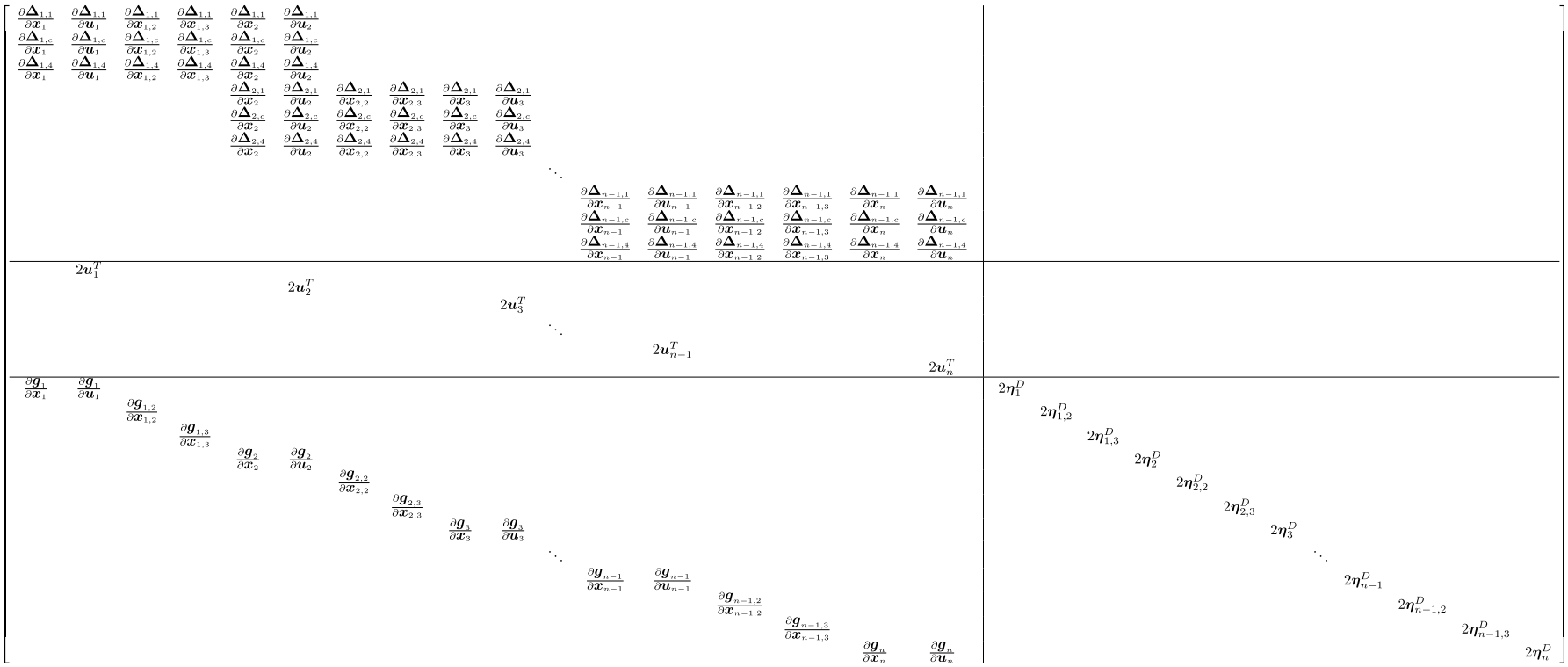

Figure 15. General Form of the Gauss-Lobatto Jacobian Matrix $D\boldsymbol{F}$ for $l = 0$, where $(\cdot)^D = \mathbf{diag}\,(\cdot)$.